

REPORT DOCUMENTATION PAGE				<i>Form Approved</i> OMB No. 0704-0188	
Public reporting burden for this collection of information is estimated to average 1 hour per response, including the time for reviewing instructions, searching existing data sources, gathering and maintaining the data needed, and completing and reviewing this collection of information. Send comments regarding this burden estimate or any other aspect of this collection of information, including suggestions for reducing this burden to Department of Defense, Washington Headquarters Services, Directorate for Information Operations and Reports (0704-0188), 1215 Jefferson Davis Highway, Suite 1204, Arlington, VA 22202-4302. Respondents should be aware that notwithstanding any other provision of law, no person shall be subject to any penalty for failing to comply with a collection of information if it does not display a currently valid OMB control number. PLEASE DO NOT RETURN YOUR FORM TO THE ABOVE ADDRESS.					
1. REPORT DATE (DD-MM-YYYY) 19-09-2003		2. REPORT TYPE Technical Paper		3. DATES COVERED (From - To)	
4. TITLE AND SUBTITLE Matrix Isolation Spectroscopy of H ₂ O, D ₂ O, and HDO in Solid Parahydrogen				5a. CONTRACT NUMBER	
				5b. GRANT NUMBER	
				5c. PROGRAM ELEMENT NUMBER	
6. AUTHOR(S) Mario Fajardo, Simon Tam, Michelle E. DeRose (AFRL/PRSP)				5d. PROJECT NUMBER 2302	
				5e. TASK NUMBER M2C8	
				5f. WORK UNIT NUMBER	
7. PERFORMING ORGANIZATION NAME(S) AND ADDRESS(ES) Air Force Research Laboratory (AFMC) AFRL/PRSP 10 East Saturn Blvd. Edwards AFB CA 93524-7680				8. PERFORMING ORGANIZATION REPORT NUMBER AFRL-PR-ED-TP-2003-237	
9. SPONSORING / MONITORING AGENCY NAME(S) AND ADDRESS(ES) Air Force Research Laboratory (AFMC) AFRL/PRS 5 Pollux Drive Edwards AFB CA 93524-7048				10. SPONSOR/MONITOR'S ACRONYM(S)	
				11. SPONSOR/MONITOR'S NUMBER(S) AFRL-PR-ED-TP-2003-237	
12. DISTRIBUTION / AVAILABILITY STATEMENT Approved for public release; distribution unlimited.					
13. SUPPLEMENTARY NOTES For presentation in the journal "Molecular Spectroscopy."					
20031017 100					
14. ABSTRACT					
15. SUBJECT TERMS					
16. SECURITY CLASSIFICATION OF:			17. LIMITATION OF ABSTRACT	18. NUMBER OF PAGES	19a. NAME OF RESPONSIBLE PERSON Leilani Richardson
a. REPORT Unclassified	b. ABSTRACT Unclassified	c. THIS PAGE Unclassified	A	48	19b. TELEPHONE NUMBER (include area code) (661) 275-5015

Matrix Isolation Spectroscopy of H₂O, D₂O, and HDO in Solid Parahydrogen

Mario E. Fajardo^a, Simon Tam^b, and Michelle E. DeRose
Propulsion Directorate, US Air Force Research Laboratory
AFRL/PRSP, Bldg. 8451, Edwards AFB, CA 93524-7680

Submitted to J. Mol. Spectrosc. _____, Received _____, Accepted _____

^a Author to whom all correspondence should be addressed.

Present address: U.S. Air Force Research Laboratory, AFRL/MNME,
2306 Perimeter Road, Eglin AFB, FL 32542-5910

Electronic mail: mario.fajardo@eglin.af.mil

^b Present address: KLA-Tencor Corp., 1 Technology Drive, Milpitas, CA 95035

Running title: "H₂O, D₂O, AND HDO IN SOLID PARAHYDROGEN"

ABSTRACT

We present infrared (IR) absorption spectra over the 800-7800 cm^{-1} region of cryogenic parahydrogen (pH_2) solids doped with H_2O , D_2O and HDO molecules. Analysis of the rovibrational spectra of the isolated H_2O , D_2O and HDO monomers reveals their existence as very slightly hindered rotors, typically showing only 2 to 5 % reductions in rotational constants relative to the gas phase. The nuclear spin conversion (NSC) of metastable $J = 1$ ortho- H_2O (oH_2O) and para- D_2O (pD_2O) molecules follow first order kinetics, with single exponential decay lifetimes at $T = 2.4$ K of 1900 ± 100 s, and 860 ± 50 s, respectively. We report without discussion some absorptions of water clusters produced during sample annealing. We report and assign a number of absorptions to oH_2 -water pairs or "complexes." The main features of the oH_2 - H_2O and oH_2 - D_2O spectra are explained qualitatively by assuming a semi-rigid C_{2v} structure with the oH_2 acting as a proton donor to the O atom. Surprisingly, NSC of oH_2 -water complexes proceeds at very nearly the same rate as for the corresponding water monomer. We report unassigned spectra of larger $(\text{oH}_2)_n$ -water clusters, and the even more surprising observation of the prolonged survival of oH_2O and pD_2O molecules clustered with several oH_2 molecules. We report and assign a number of water dopant-induced IR absorption features of the pH_2 host, along with cooperative water- pH_2 transitions in which the vibrational excitation of the pH_2 solid is accompanied by a pure rotational transition of the water dopant.

Keywords:

matrix isolation spectroscopy; solid parahydrogen; nuclear spin conversion; dopant-induced IR activity; cooperative absorption

I. INTRODUCTION

The Winnewissers' solid hydrogen spectroscopic opus (1-6) has yielded the discovery of several new rovibrational transitions, including the novel class of condensed phase "triple transitions," in which three hydrogen molecules cooperate to absorb a single photon (6). Their application of high-resolution high-sensitivity Fourier transform infrared (FTIR) spectrometry has produced an extensive compilation of observations, covering most of the 600-14000 cm^{-1} region, which are unparalleled in their internal self-consistency. This comprehensive spectral survey, alongside a handful of classic prior solid parahydrogen (pH_2) spectroscopic studies (7-13), constitute an indispensable resource to those seeking an improved understanding of photodynamics in quantum molecular solids -- including the growing number of practitioners of Matrix Isolation Spectroscopy (MIS) in solid pH_2 matrices.

The use of pH_2 solids with very low residual orthohydrogen (oH_2) concentrations as matrix hosts for chemically interesting dopants originated in the Oka laboratory in Chicago, and has advanced in collaboration with Shida and Momose and coworkers in Kyoto (14-24). These authors have reviewed in detail the unique properties of solid pH_2 as a matrix host, including the preservation of the spherical nature of the ground state ($v = 0, J = 0$) pH_2 molecules in the solid phase, and the resulting advantages to high resolution rovibrational spectroscopy (14,16). Most of the samples utilized in these pioneering studies were produced by condensation of a room temperature dopant/ pH_2 gas mixture in an enclosed cell held near $\frac{1}{2}$ the pH_2 triple point temperature of $T_{\text{tp}} = 13.8$ K. This approach results in beautifully transparent, centimeters-long, polycrystalline samples which are stable over a relatively broad temperature range. Unfortunately, this sample preparation scheme also leads to extensive dopant aggregation, clustering, and even phase separation.

A few years ago we developed a modification to the standard MIS substrate-in-vacuum sample deposition scheme which yields optically transparent, millimeters-thick, doped pH_2 solids, and which is compatible with most existing impurity doping methods. Our Rapid Vapor Deposition (RVD) technique (25,26), in which volatilized dopants are co-deposited with an independent flow of precooled pH_2 gas directly onto a substrate-in-vacuum held at $T \approx 2$ K, offers excellent dopant isolation efficiencies for concentrations up to ~ 100 ppm -- ideal for FTIR-based absorption diagnostics. However, this improved isolation efficiency comes at the price of a more complicated host morphology with higher defect concentrations, and a maximum

working temperature limited by destructive sample sublimation to $T < 5$ K (23,27). Despite these shortcomings, we are aware of a number of ongoing efforts in independent laboratories to adapt the basic RVD scheme to a variety of MIS applications.

Since water vapor is the major residual gas component in the unbaked o-ring sealed high-vacuum systems typically employed in MIS studies, water is a ubiquitous impurity in vapor deposited cryogenic matrices; appearing unintentionally in our RVD pH_2 solids at up to ~ 1 ppm levels (28). Clearly, *a priori* knowledge of the spectroscopic features attributable to the pH_2 host, and to water molecules and other likely contaminants (29), is required to avoid confusion while assigning spectra of new species in solid pH_2 , *e.g.* dopant- H_2 reaction products (30,31). Also, water clusters and water complexes with other dopants are of fundamental interest (28); the process of analyzing their spectroscopic signatures also begins with the identification and elimination of matrix host features, and more mundane water related features. We hope that the data presented in this manuscript will facilitate this process.

In what follows we give a brief review of the rovibrational spectroscopy of matrix isolated H_2O , D_2O , and HDO molecules, we summarize past lessons learned about the microscopic structure of RVD pH_2 solids, along with a few salient details of the gas phase spectroscopy of water molecules. We describe our experimental implementation of the RVD sample preparation technique, and our FTIR spectroscopic diagnostics covering the $800\text{--}7800\text{ cm}^{-1}$ range. We present and assign the direct IR absorptions of water monomers isolated in solid pH_2 , including data showing the kinetics of nuclear spin conversion (NSC) of metastable $J = 1$ ortho- H_2O (oH_2O), para- D_2O (pD_2O), and oH_2 molecules. We discuss the observed matrix effects on the water monomer spectra, *i.e.* gas-to-matrix vibrational band origin shifts and perturbed rotational bands. We assign a few transitions to water molecules with a single oH_2 nearest neighbor, *i.e.* " oH_2 - H_2O complexes," and present unassigned spectra of larger $(oH_2)_n$ -water clusters along with a qualitative description of the observed features, including NSC in oH_2 -water complexes and $(oH_2)_n$ -water clusters. Finally, we present and discuss IR features of the pH_2 solid induced by the presence of the water dopants, as well as cooperative absorption features which arise when the dopant and the pH_2 solid share the energy of a single IR photon (32-34).

II. BACKGROUND

A. Matrix Isolation Considerations

As might be expected, studies of trapped water monomers date back to the origins of the MIS field (35-51). Rovibrational spectra of water monomers in rare gas solids (RGS) are well explained by assuming that the water molecules exist as slightly hindered rotors in single substitutional vacancies (37-41,48-51), except for a few features assigned to "non-rotating" water molecules trapped near defects (38,39,50,51). Water monomers trapped in molecular solids such as N₂ and normal-D₂ do not rotate (42-47); apparently the trapping environments in these solids are significantly more anisotropic than those in RGS. With two important exceptions (*i.e.* clustering with residual oH₂, and the dopant-induced and cooperative transitions associated with the pH₂ vibron) the spectroscopy of water monomers in solid pH₂ is understandable by comparison with this earlier RGS work.

Since the center of mass separation in the gas phase H₂-H₂O complex is $R_e \approx 3.6 \text{ \AA}$ (52), and the nearest neighbor separation in solid pH₂ is $R_{nn} = 3.789 \text{ \AA}$ (10), a water molecule should be readily accommodated in a single substitutional vacancy in solid pH₂. Spectra of other dopants in RVD solid pH₂ have been well explained by postulating that our as-deposited solids exhibit a mixed hexagonal-close-packed/face-centered-cubic (hcp/fcc) polycrystalline morphology (25,27,29); the crystal field in single substitutional hcp sites is of D_{3h} symmetry (16), while fcc sites are of O_h symmetry (27). However, the hcp (...ABCABC...) and fcc (...ABABAB...) structures are only two of the infinite number of densest close-packed structures derivable by stacking of close-packed planes (53). If only nearest neighbor dopant-pH₂ interactions are important, dopants in single substitutional sites in layers B will exist in regions of local hcp stacking (...XABCX..., "hcp-like") or local fcc stacking (...XABAX..., "fcc-like"). Thus, we cannot rigorously exclude structures based on other stacking arrangements, such as polytypic or random-stacked close-packed (rcp) structures. Annealing of RVD pH₂ samples at $T > 4.5 \text{ K}$ results in nearly complete and irreversible conversion to the thermodynamically stable hcp structure. We show below that annealing of water doped pH₂ solids results in only minor shifts in peak positions, but often in considerable sharpening of the linewidths.

B. Gas Phase Water Molecules

The molecular symmetry point group for H₂O and D₂O molecules is C_{2v}, hence all three

principal moments of inertia $I_A < I_B < I_C$ are different, the three corresponding rotational constants $A > B > C$, are different, and these molecules exist as asymmetric tops (54). The C_2 symmetry axis is the intermediate B axis, the A axis lies in the plane of the molecule, and the C axis is mutually perpendicular (55). FIG. 1 shows a few germane rovibrational energy levels and allowed IR transitions for gas phase H_2O and D_2O molecules (37,54). For symmetric tops the rotational levels are labeled by the quantum numbers J and K, where J is the total rotational angular momentum, and K is the constant component of J about the figure axis (54). The H_2O and D_2O asymmetric rotor levels are labeled $J_{K_a K_c}$, where $K_a = |K|$ correlated to the prolate rotor limit ($I_B = I_C$), and $K_c = |K|$ in the oblate rotor limit ($I_A = I_B$) (56). Alternatively, the levels can be labeled J_τ , where $\tau = K_a - K_c$, and $-J \leq \tau \leq J$, with τ increasing with increasing level energy. Each of these levels is $(2J + 1)$ -fold degenerate in the quantum number M arising from the isotropy of free space.

The two hydrogenic atoms are equivalent via the C_2 symmetry axis, so just as in the case of H_2 and D_2 (10) the H_2O and D_2O molecules each exist in two distinct nuclear spin ($I = I_1 + I_2$) modifications (54): para- H_2O (pH_2O , $I = 0$), ortho- H_2O (oH_2O , $I = 1$), ortho- D_2O (oD_2O , $I = 0, 2$), and para- D_2O (pD_2O , $I = 1$), where by convention the modification with the highest degeneracy $g_I = \Sigma(2I + 1)$ is designated "ortho." At liquid helium (lHe) temperatures the molecules rapidly relax to the lowest rotational level available while conserving I: the true ground 0_{00} state for pH_2O and oD_2O , and the metastable 1_{01} state for oH_2O and pD_2O .

The three nondegenerate vibrational fundamentals are labeled ν_1 (symmetric stretch), ν_2 (bend), and ν_3 (asymmetric stretch). Rovibrational transitions of asymmetric top molecules are classified as Type A, Type B, or Type C, depending on whether the transition dipole moment is in the direction of the least, intermediate, or largest moment of inertia, respectively (54). Thus, excitation of the ν_1 , ν_2 , and ν_3 fundamentals, and all overtones and combination bands, are further classified as Type A bands if $\Delta \nu_3$ is odd, or Type B otherwise (54). The operant IR selection rules are summarized implicitly in FIG. 1 as arrows showing the relevant dipole allowed transitions. The gas phase level energies, transition wavenumbers, and transition probabilities are taken from the literature (57-62).

The H and D atoms in HDO are trivially nonequivalent, hence there is no ortho/para distinction, and all HDO molecules can relax at low temperatures to the 0_{00} state. The molecular symmetry point group for HDO is C_1 , and the vibrational modes change character qualitatively,

with the ν_1 mode resembling a localized O-D stretch, and the ν_3 mode a localized O-H stretch (54,63,64); so any HDO molecule can participate in mixed Type A and Type B transitions. For HDO, the compilation of gas phase transition probabilities in the HITRAN database (59) was especially helpful for clarifying which transitions should be observable in our experiments.

III. EXPERIMENTAL

Our experimental methods have been described in detail before (25,26). Briefly: we prepare our samples by co-deposition of independent flows of room temperature water vapor and precooled $p\text{H}_2$ gas onto a BaF_2 substrate-in-vacuum cooled to $T \approx 2$ K in a ^4He bath cryostat. We estimate the dopant concentrations from these gas flow rates (with a ± 50 % uncertainty in these experiments due to water adsorption/desorption within the gas handling manifold) and so report them here using only one significant digit. In these experiments we operate our ortho/para H_2 converter at $T = 15$ K, yielding ≈ 100 ppm residual $o\text{H}_2$ content, and at $T = 19$ K yielding ≈ 1000 ppm residual $o\text{H}_2$. Our favorite 200 mmol/hour $p\text{H}_2$ gas flow rate results in a solid growth rate of ≈ 3 mm/hour. We determine the sample thickness (65) within ± 10 % from the intensities of the $Q_1(0)+S_0(0)$ and $S_1(0)+S_0(0)$ double transitions (66) of the $p\text{H}_2$ host.

We measure IR absorption spectra of our samples across the 800 to 7800 cm^{-1} range using an FTIR spectrometer (Bruker IFS120HR) equipped with glowbar and tungsten lamp sources, Ge:KBr and Si:CaF_2 beamsplitters, and liquid nitrogen cooled HgCdTe and InSb detectors. To accommodate the IR diagnostic, the entire optical path is enclosed within a 0.5 m^3 polycarbonate box purged with a constant flow of dry nitrogen gas. During the FT process, we employ a triangular apodization function which results in a $\sin^2(x)/x^2$ instrumental lineshape function (67).

In this study we produce samples and collect IR data following two different experimental protocols: (1) our standard approach of depositing a ≈ 3 mm thick sample over an hour long period, then collecting and co-adding several large interferograms over an additional hour to yield high resolution (0.005 to 0.01 cm^{-1}) spectra, and (2) depositing thinner samples in 10 to 15 minutes followed immediately by the rapid accumulation of shorter interferograms over just 2 minutes to yield low resolution (0.05 to 0.1 cm^{-1}) spectra favoring the observation of IR transitions of metastable $J = 1$ water molecules. Individual sample preparation details are given in the figure captions.

IV. RESULTS & DISCUSSION

A. H_2O Monomers

FIG. 2 shows IR absorption spectra in the ν_2 H_2O region; a summary of the observed peak positions, linewidths, and assignments can be found in Table 1. We make our assignments by comparison with previous gas phase and MIS studies; the monomer peak positions in solid pH_2 are uniformly red shifted by only $\approx 4 \text{ cm}^{-1}$ from the gas phase values. The $oH_2O \rightarrow pH_2O$ NSC process results in diminishing intensities for absorptions originating from the 1_{01} rotational level, and growth of those from the 0_{00} level; we will discuss the decay kinetics in greater detail, below. We will also show below that the sharp features in FIG. 2 labeled with an "o" grow in number and intensity with the deliberate addition of oH_2 , so we assign these features to oH_2 - H_2O complexes, or possibly larger $(oH_2)_n$ - H_2O clusters, identifying oH_2O and pH_2O where possible. Not shown are spectra of the other Type B bands of H_2O observed in this study, $2\nu_2$ and ν_1 , which demonstrate similar behavior; these data are also summarized in Table 1.

Each of the H_2O monomer features in FIG. 2 appears to be a broad single line; we observe no lifting of the M degeneracy of the excited rotational levels by the crystal field. While the rather broad lines make it dangerous to dismiss inhomogeneous contributions to the linewidths, we note that annealing of this sample results in shifting and sharpening of the $1_{11} \leftarrow 0_{00} \nu_2$ H_2O line by only $\sim 0.1 \text{ cm}^{-1}$. The nearly Lorentzian lineshapes of the $1_{11} \leftarrow 0_{00}$ and $2_{12} \leftarrow 1_{01} \nu_2$ H_2O features are suggestive of the rovibrational dephasing reported for CD_4 in solid pH_2 (21). Focusing further to the $1_{11} \leftarrow 0_{00}$ feature, the measured annealed linewidth of γ (FWHM) = 1.6 cm^{-1} can be related to a dephasing time (21) of $T_2 = 1/(\pi c \gamma) \approx 7 \text{ ps}$, which is only a few times the classical rotational period in the 1_{11} state: $T_{\text{rot}} = 1/c(A + C) \approx 1 \text{ ps}$.

Annealing also leads to new sharp features in the 1595 - 1600 cm^{-1} region, and to a broad peak centered at 1605 cm^{-1} ; we tentatively assign these features to water clusters. Such water cluster features will be noted without significant discussion throughout this manuscript.

FIG. 3 shows IR absorption spectra in the ν_3 H_2O region; again peak positions, widths, and assignments can be found in Table 1. We discussed briefly these ν_3 H_2O monomer peaks in a communication concerning water clusters in solid pH_2 (28); also, the $1_{01} \leftarrow 0_{00}$ peak near 3765.5 cm^{-1} was reported as the signature of a H_2O photoproduct in $HI/CO_2/pH_2$ samples (20). Another prior report of H_2O peak positions in solid pH_2 lists line positions which differ considerably from

ours (22); perhaps due to perturbations by the ionic species known to be present in those samples.

As in the case of the ν_2 H₂O band, we again observe single Lorentzian peaks for each monomer transition, the decay of oH₂O absorptions occurs on the ~ 1 hour timescale of the experiment, we note several features attributable to oH₂-H₂O complexes or (oH₂)_n-H₂O clusters, and peaks due to water clusters appear upon annealing near 3716, 3725, 3738.3, and 3744.6 cm⁻¹. Not shown are spectra of the other similarly behaving Type A H₂O bands: $\nu_2+\nu_3$, $2\nu_2+\nu_3$, and $\nu_1+\nu_3$; these data are also included in Table 1.

In comparison with the lower energy ν_1 and ν_2 H₂O bands, the two main features of the ν_3 H₂O band are quite sharp, suggesting order-of-magnitude longer rovibrational dephasing times. This observation contradicts the rough rule of thumb, proposed based on previously reported spectra of dopants in solid pH₂, that the lowest energy vibrational mode should show the narrowest lines for a given dopant molecule. This hypothesis was consistent with the picture of intramolecular vibrational redistribution, "IVR" (68), playing an important role in relaxing the higher lying vibrational modes. Our H₂O/pH₂ observations indicate faster dephasing of Type B bands by dopant-host interactions than of Type A bands by IVR.

We note in passing the momentary confusion caused by the near coincidence of the Q₁(0)+U₀(0) H₂ double transition (9), which we observe at 5320.0 cm⁻¹, with the $\nu_2+\nu_3$ H₂O combination band vibrational origin.

B. D₂O Monomers

A summary of our D₂O/pH₂ data and assignments is given in Table 2. FIG. 4 shows the ν_2 D₂O spectral region which is very similar to the ν_2 H₂O spectra, except: it is more spectrally compact due to the smaller rotational constants of D₂O, the $1_{10} \leftarrow 1_{01}$ ν_2 D₂O line is very much sharper than for ν_2 H₂O, and the decay of metastable J = 1 D₂O molecules is more than twice as fast as for J = 1 H₂O. FIG. 4 also shows another example of an intruding solid hydrogen line: U₀(0) H₂ near 1167.1 cm⁻¹; the increase in intensity of this feature upon annealing reflects the irreversible fcc \rightarrow hcp conversion of the pH₂ host. Clustering of D₂O molecules upon annealing leads to new sharp peaks near 1180 and 1190 cm⁻¹.

FIG. 5 shows the ν_3 D₂O region which again resembles a more spectrally compact version of

the ν_3 H₂O region, except that the lines are considerably sharper in the annealed spectrum. In fact, upon annealing the $1_{01} \leftarrow 0_{00}$ ν_3 D₂O line sharpens to 0.10 cm⁻¹ FWHM, and one of the oH₂-oD₂O features actually split into a triplet at 2785.05, 2785.15, and 2785.29 cm⁻¹. We also note the strange temporal dependence of the peak near 2769.3 cm⁻¹, which we assign to an oH₂-pD₂O complex, but which does not follow the decay kinetics of pD₂O. This feature is only present in D₂O doped samples, so it is not a transition of the pH₂ host; we speculate that it may overlap a (D₂O)_n cluster line, such as the ones apparent near 2751, 2764, and 2776 cm⁻¹.

C. Nuclear Spin Conversion of Isolated H₂O & D₂O Monomers

FIG. 6 plots the integrated intensities of a few transitions of $J = 1$ H₂O and D₂O monomers vs. time after sample deposition. We present only those peaks which do not overlap water cluster features and so decay cleanly to zero baseline. At $T = 2.4$ K, the oH₂O population decays as a single exponential with a lifetime of 1900 ± 100 s, the pD₂O population decays as a single exponential with a lifetime of 860 ± 50 s. Not shown are plots of the growth of the $J = 0$ water monomer transitions which show the same single exponential first order kinetics. We did not investigate the temperature dependence of these NSC rates, nor any possible photo-effects due to room lights or the IR radiation from the spectrometer.

Previous studies of NSC of H₂O in solid Ar matrices (39,41) reported much longer conversion times than ours, unless an O₂ dopant was deliberately added at 0.1 - 1 % concentrations. Those authors concluded that interactions with the paramagnetic O₂ molecules accelerate the rate of decay of oH₂O; we do not believe that O₂ impurities play any role in our experiments. Based on the measured composition of residual gases in our cryostat prior to cooldown, we expect O₂ contamination to be smaller than H₂O contamination by at least a factor of 10; putting an upper bound on trapped O₂ concentrations of ~ 100 ppb. Furthermore, we do not see any spectroscopic evidence for O₂-H₂O complexes, while we clearly do so for oH₂-H₂O complexes (*vide infra*).

Our results more closely resemble those reported for NSC of CH₄ molecules in solid pH₂ where clean first order kinetics were also observed (19). This study also documented a curious dependence of the NSC rate constant on the concentration of oH₂ molecules: essentially no dependence for oH₂ concentrations between 0.05 and 2 %, then a linearly increasing rate constant with oH₂ concentrations of 10 to 75 %. The authors conclude that the increased NSC

rate is due to magnetic dipole-dipole interactions between nearest neighbor oH_2 and methane molecules, but the mechanism for NSC at the lower oH_2 concentrations remains unclear (19). More recent unpublished work by this group has demonstrated the strong temperature dependence of NSC rates in low oH_2 concentration samples, indicating that interactions between the $J = 1$ water dopants and the non-magnetic pH_2 host are capable of promoting the NSC process (69).

Since the oH_2 concentrations in the samples depicted in FIGS. 2-6 are only 100 ppm, and with the benefit of clear spectroscopic signatures of isolated water monomers as distinct from oH_2 -water complexes, we assert that our reported NSC lifetimes are indeed for oH_2O and pD_2O molecules having no oH_2 nearest neighbors. These data may provide a valuable test for models of NSC invoking "non-magnetic" mechanisms (70-72). We will discuss the NSC of $(\text{oH}_2)_n$ - oH_2O clusters further below.

D. HDO Monomers

A summary of HDO/ pH_2 peak positions, linewidths, and assignments appears in Table 3. FIG. 7 shows the ν_2 HDO region of the IR spectrum of a mixed $\text{H}_2\text{O}/\text{HDO}/\text{D}_2\text{O}/\text{pH}_2$ sample which is dominated by two monomer peaks, which we assign to the $1_{01} \leftarrow 0_{00}$ and $1_{11} \leftarrow 0_{00}$ transitions based on their 2 to 3 cm^{-1} gas-to-matrix red shifts; these shifts being intermediate between those observed for ν_2 H_2O and ν_2 D_2O features. Since HDO does not exist in ortho/para modifications, at $T = 2.4$ K we expect 99.99 % of the HDO molecules to rapidly relax to the ground 0_{00} ($v = 0$) level. Using the gas phase rotational excitation energy for the 1_{01} ($v = 0$) level of ≈ 15.5 cm^{-1} , we predict a 100 x increase in thermal population for warming from $T = 2.4$ K to $T = 4.8$ K. Indeed, warming this sample to $T = 4.8$ K results in the appearance of the $0_{00} \leftarrow 1_{01}$ peak, again at a ≈ 3 cm^{-1} gas-to-matrix red shift. Despite comparable or even larger transition strengths (59), we observe no other ν_2 band absorptions from the 1_{01} level; these bands are either too broad or overlapped by other absorption features. Repeated temperature cycling shows these spectral changes to be completely reversible, with the exceptions of the dramatic sharpening of the absorption lines and the appearance of water cluster features near 1399 and 1407 cm^{-1} . The oH_2 -HDO complex peak at 1413.28 cm^{-1} resolves into a doublet at 1413.20 and 1413.29 cm^{-1} upon annealing.

FIG. 8. shows the ν_3 HDO region which is initially overlapped by ν_3 oH_2O and oH_2 - oH_2O

complex absorptions. We again observe a transition from the thermally populated 1_{01} level upon warming the sample to $T = 4.8$ K. Annealing again results in dramatic sharpening of the absorption lines, with the oH_2 -HDO multiplet near 3705.5 cm^{-1} resolving into a triplet of sharp (0.03 cm^{-1} FWHM) peaks at 3705.39 , 3705.44 , and 3705.53 cm^{-1} , and new water cluster features appearing near 3700 cm^{-1} .

The annealed linewidths for HDO monomers are the sharpest we have encountered for any of the water monomers, perhaps due to the qualitative differences in vibrational mode character and IVR pathways for the mixed isotopomer (54,63,64). FIG. 9 shows the effects of annealing on the $1_{01} \leftarrow 0_{00} \nu_1$ HDO line, which splits into two peaks: a main Lorentzian line at 2729.995 cm^{-1} , and a small satellite at 2730.085 cm^{-1} ; the 0.03 cm^{-1} linewidth of the main peak yields a dephasing time of $T_2 \approx 0.3 \text{ ns}$. We suggest that the main peak is due to HDO monomers in hcp-like trapping sites, and the satellite to HDO monomers in residual fcc-like trapping sites. The 0.09 cm^{-1} splitting between these peaks is consistent with our previous estimate of $\approx 0.1 \text{ cm}^{-1}$ residual inhomogeneous linebroadening of the other water monomer transitions.

E. Matrix Effects on Monomer Spectra

1. Gas-Matrix Shifts

FIG. 10 shows a correlation plot of water monomer gas-to-matrix red shifts vs. rovibrational excitation, summarizing these data from Tables 1, 2, and 3. The correlation is monotonic and roughly linear, however we can readily discern two distinct subtrends: the slope for ν_2 excitation is $(E_{\text{gas}} - E_{\text{matrix}})/E_{\text{gas}} \approx 0.002$, whereas the slope for ν_1 or ν_3 excitation is ≈ 0.0035 ; these trends are maintained for overtones and combination bands. We do not understand these trends, and present our data and reasoning here to highlight this unresolved question.

We initially expected these trends to be (at least qualitatively) easily explicable using the standard treatment of matrix shifts of the vibrational *band origins*, which assumes the separation of dopant/host intermolecular interactions into a sum of electrostatic + induction + dispersion + repulsive terms (73):

$$V = V_{\text{elec}} + V_{\text{ind}} + V_{\text{disp}} + V_{\text{rep}} \quad [1].$$

The gas-to-matrix band origin shifts are then calculated perturbatively by considering the

changes to each of these terms upon vibrational excitation of the dopant molecule. Since $J = 0$ pH_2 molecules are spherically symmetric and have no rotationally averaged permanent electrostatic multipole moments, we can safely neglect the electrostatic interaction term. The repulsive interactions are the most difficult to evaluate, and are likely to increase in magnitude upon vibrational excitation of the dopant, contributing to spectral blue shifts; we will tentatively ignore them for the moment.

The electrostatic induction solvation contribution to the vibrational band origin matrix shift is predicted to be proportional to the difference in the squares of the dopant's molecular electric dipole moment upon vibrational excitation (73):

$$\Delta_v \nu_{\text{ind}} \propto \Delta_v (\mu^2) \quad [2]$$

where: $\Delta_v (\mu^2) \equiv [\mu^2]_v - [\mu^2]_0$, and μ is the rotationless molecular electric dipole moment. The applicability of this expression to individual rovibrational transitions is suspect, due to rotational averaging of the dopant molecule's dipole moment. However, our observation of only slightly matrix perturbed rotational band structures (*vide infra*) means that the individual rovibrational transitions indeed shift with the vibrational band centers. The known vibrational dependence of μ (74,75) predicts red shifts for ν_1 and ν_3 excitation: $\Delta_v \nu_{\text{ind}} (\nu_1) \ll \Delta_v \nu_{\text{ind}} (\nu_3)$ and a blue shift (*i.e.* a decrease in $|\mu|$) upon ν_2 excitation, so induction interactions alone cannot explain the observed trends in matrix shifts. Furthermore, this discrepancy cannot be explained by rotational averaging effects, as the ν_1 and ν_2 bands share the same rotational structure.

The vibrational band matrix shift due to changes in dispersion energies is proportional to the change in the dopant's molecular polarizability upon excitation (73):

$$\Delta_v \nu_{\text{disp}} \propto \Delta_v (\alpha) \quad [3]$$

where: $\Delta_v (\alpha) \equiv [\alpha]_v - [\alpha]_0$, and α is the mean H_2O polarizability. The vibrational dependence of the mean polarizability of H_2O (76) predicts $\Delta_v \nu_{\text{disp}} (\nu_1) \approx \Delta_v \nu_{\text{disp}} (\nu_2) < \Delta_v \nu_{\text{disp}} (\nu_3)$, which again incorrectly places the contribution from excitation of the ν_1 symmetric stretch mode well below that for the ν_3 asymmetric stretch mode.

We see that neither the induction or dispersion contributions, either singly or in combination, can explain the details of the observed matrix shifts. A proper calculation will likely involve a combination of all the interactions in the standard model, including the repulsive interactions and perhaps even more subtle effects such as hydrogen-bonding H₂-H₂O interactions, which is beyond the scope of the present study.

2. Rotational Analysis

Since we only observe IR transitions originating from the 0₀₀ and 1₀₁ rotational levels in the vibrational ground state for H₂O, D₂O, and HDO monomers, we have very limited information with which to conduct a rotational analysis. We did observe a handful of transitions originating in a common 1₀₁ lower state, which yields a few rotational level splittings in the vibrationally excited states; these data are summarized in Table 4. We employ the Mecke sum rules for the rigid asymmetric top (54) to recast the observed energy splittings as sums of rotational constants. We note a small (and given the large widths of the observed absorption features perhaps not significant) gas-to-matrix *increase* in the splittings between the 2₁₂ and 1₁₀ rotational levels (*i.e.* in the C rotational constant) in the excited ν_2 and ν_1 vibrational states for H₂O; all other measured splittings and rotational constant sums showed modest 2 to 5 % decreases.

We were also able to bracket the vibrational origin for a number of transitions. We define an energy difference equal to the sum of the rotational energies of the 1₀₁ level in the ground and vibrationally excited states:

$$\Delta E_{\text{asym}} \equiv \bar{\nu} [1_{01} \leftarrow 0_{00}] - \bar{\nu} [0_{00} \leftarrow 1_{01}] \quad [4]$$

where $\bar{\nu}$ signifies the transition wavenumber of the $\Delta v = +1$ vibrational excitation accompanied by the bracketed rotational transition. We can adapt the Mecke sum rules to estimate vibrationally averaged rotational constants:

$$\Delta E_{\text{asym}} = (B + C)_{v=1} + (B + C)_{v=0} = 2 (B + C)_{\text{avg}} \quad [5].$$

These results are summarized in Table 5 which shows a consistent ≈ 3 % gas-to-matrix reduction, again validating our picture of water monomers in solid pH₂ existing as very slightly

hindered rotors.

F. oH₂-oH₂O Complexes and (oH₂)_n-water Clusters

We confirm the identification of the features labeled with an "o" in FIGS. 2-8 to absorptions of oH₂-oH₂O complexes and (oH₂)_n-H₂O clusters by deliberately doping some samples with \approx 1000 ppm oH₂, which we accomplish by operating the ortho/para converter at $T = 19$ K. Spectra of the ν_2 H₂O region are shown in FIG. 11, and spectra of the ν_3 H₂O region are shown in FIG. 12. The features appearing at the lowest oH₂ concentrations are tentatively attributed in Tables 1-3 to oH₂-H₂O complexes, although some of the weaker features may well be due to water clustering with multiple oH₂ molecules.

We note in passing that (assuming preservation of natural isotopic abundances) these pH₂ solids also contain \approx 300 ppm of a benign and immobile HD impurity, which rapidly relaxes to $J = 0$ upon cooling, making it virtually indistinguishable from the pH₂ host molecules. In contrast, oH₂ molecules have a nonzero rotationally averaged electrostatic quadrupole moment (10), so they can interact more strongly with dopant molecules than can the spherically symmetric $J = 0$ pH₂ molecules, resulting in some clustering during the deposition process. Also, oH₂ molecules are mobile through the pH₂ solid by a process known as "quantum rotational diffusion" in which an oH₂-pH₂ nearest neighbor pair converts into a pH₂-oH₂ pair (8,10).

The cleanest examples of the spectroscopic consequences of oH₂-dopant clustering are found in a recent report on (oH₂)_n-CH₃F clusters in solid pH₂ (77). CH₃F does not rotate in solid pH₂, so the rovibrational spectrum of the ν_3 C-F stretching mode collapses to a single line at the vibrational band origin. The quadrupolar oH₂ molecules bind strongly to the electrostatic dipole of the non-rotating CH₃F molecule, and each of the 13 observed spectral features can be associated with a CH₃F molecule with from 0 to 12 oH₂ nearest neighbors.

At first glance the spectra of (oH₂)_n-H₂O clusters in the ν_2 H₂O region appear to tell a similar story. The inset to FIG. 11 shows the detail near the ν_2 H₂O vibrational origin where the intensity and number of features increase with addition of oH₂, however not in a neat countable fashion as for (oH₂)_n-CH₃F. The sharp features near the vibrational origin are indeed evocative of the "non-rotating" water absorptions reported for water molecules trapped near defects in RGS (42-47). This "strictly non-rotating" interpretation requires that the anisotropy of the trapping environment for an H₂O molecule adjacent to even a single oH₂ molecule be large

enough to completely quench the H_2O rotation, leaving it to oscillate about some space-fixed equilibrium orientation (78). In this limit, angular momentum is conserved at the level of the solid as a whole, and the dopant angular momentum quantum numbers become moot. Indeed, the total integrated intensity for the $\text{oH}_2\text{-H}_2\text{O}$ complex peaks in the 1593 to 1595 cm^{-1} region in FIG. 11(a) decays much more slowly (only about 10 % in 1 hour) than do the oH_2O monomer features, and obviously do not grow in the manner of pH_2O monomers, suggesting either (1) that the $\text{oH}_2\text{-oH}_2\text{O}$ and $\text{oH}_2\text{-pH}_2\text{O}$ spectroscopic features overlap, or perhaps (2) that there is no surviving distinction between $\text{oH}_2\text{-oH}_2\text{O}$ and $\text{oH}_2\text{-pH}_2\text{O}$ complexes.

This appealingly simple interpretation is refuted by the spectra in FIG. 12, which show the qualitatively different behavior of the $\nu_3\text{ H}_2\text{O}$ band upon addition of oH_2 . In this case we see very little IR activity at the vibrational band origin, and instead observe progressions of peaks building inwards from each of the H_2O monomer $1_{01} \leftarrow 0_{00}$ and $0_{00} \leftarrow 1_{01}$ transitions. In fact, the features at 3725.46 and 3758.46 cm^{-1} appear at low oH_2 concentrations, and display the same NSC kinetics as the nearby water monomer transitions (*vide infra*), suggesting that they correspond to absorptions of $\text{oH}_2\text{-oH}_2\text{O}$ and $\text{oH}_2\text{-pH}_2\text{O}$ complexes, respectively.

We can harmonize the observations for the $\nu_2\text{ H}_2\text{O}$ and $\nu_3\text{ H}_2\text{O}$ bands by incorporating elements of what is known about gas phase $\text{H}_2\text{-H}_2\text{O}$ complexes, taking into account a couple of obvious and subtle condensed phase effects. The ground state of the gas phase $\text{pH}_2\text{-H}_2\text{O}$ complex resembles the $\text{Ar-H}_2\text{O}$ complex and is best described as a pseudo-diatomic with very slightly hindered rotation of the H_2O subunit (52). The ground state of the gas phase $\text{oH}_2\text{-H}_2\text{O}$ complex exhibits a nontrivial barrier to in-plane rotation of the H_2O subunit, with an equilibrium geometry resembling the minimum energy "H₂O proton acceptor" C_{2v} configuration in which the H_2 bond points along the C_2 symmetry axis towards the O atom (52). However, large amplitude internal rotor dynamics of the H_2 and H_2O subunits results in: (1) a ground state $\text{oH}_2\text{-pH}_2\text{O}$ wavefunction with the H_2 molecule being only ≈ 8 times more likely to be on the O side than the H side of H_2O , and (2) a node at the C_{2v} geometry for the lowest energy $\text{oH}_2\text{-oH}_2\text{O}$ state, precluding an accurate assignment of the gas phase spectra using a semirigid C_{2v} asymmetric top model (52).

The most obvious consequence of the matrix "cage effect" on an $\text{oH}_2\text{-H}_2\text{O}$ complex trapped in solid pH_2 is quenching of the end-over-end rotation of the complex relative to the crystal lattice; although "internal" rotation and reorientation of the oH_2 and H_2O subunits may not be

strongly perturbed. Additionally, axial confinement of the oH₂ and H₂O subunits could reduce their average separation, leading to increased anisotropic interactions.

A more subtle matrix effect is the partial cancellation of oH₂-H₂O anisotropic interactions by pH₂-H₂O interactions in the highly symmetrical trapping environment (15). This is imperfectly illustrated by considering the net anisotropic potential for rotation of H₂O within a linear oH₂-H₂O-pH₂ construct. More formally, the anisotropic potential experienced by an H₂O molecule in an oH₂-H₂O complex trapped in solid pH₂ can be written in analogy to Ref. (15) as:

$$V_{\text{aniso}} = V_{\text{oH}_2}(\mathbf{R}_1, \Omega_1, \omega) + \sum_{i>1} V_{\text{pH}_2}(\mathbf{R}_i, \Omega) \quad [6]$$

where the H₂O molecule occupies the coordinate system origin, the oH₂ molecule sits at position \mathbf{R}_1 with orientation Ω_1 in the crystal frame, ω is the orientation of the H₂O molecule relative to the oH₂-H₂O pair axis and Ω the H₂O orientation relative to the crystal frame, and the remaining pH₂ neighbors sit at positions \mathbf{R}_i . The partial cancellation effect is most clearly represented by adding and subtracting the interactions of a hypothetical extra pH₂ molecule at the oH₂ site \mathbf{R}_1 (15):

$$V_{\text{aniso}} = V_{\text{oH}_2}(\mathbf{R}_1, \Omega_1, \omega) - V_{\text{pH}_2}(\mathbf{R}_1, \omega) + \sum_i V_{\text{pH}_2}(\mathbf{R}_i, \Omega) \quad [7]$$

or:

$$V_{\text{aniso}} = \Delta V_{\text{oH}_2\text{-pH}_2}(\mathbf{R}_1, \Omega_1, \omega) + V_{\text{crystal}}(\Omega) \quad [8]$$

where $\Delta V_{\text{oH}_2\text{-pH}_2}$ is the difference in anisotropic interactions between an oH₂-H₂O and a pH₂-H₂O pair, and V_{crystal} is the pure crystal field term.

Because of the cage effect, the partial cancellation effect, and the pure crystal field term, we cannot adopt unmodified the rotational dynamics and spectroscopic features of the gas phase oH₂-H₂O complexes to explain our condensed phase situation. In the language of Ref. (52), these additional interactions would modify the magnitude of the angular anisotropy parameter, ζ , connecting the free H₂O rotor ($\zeta = 0$) and strongly hindered rotor ($\zeta = 1$) limits. It is difficult to judge whether the net effect would be to increase or decrease ζ ; the required condensed phase simulations are beyond the scope of this study, so we abandon any quantitative assignment of the

oH_2 -water complex spectra.

However, by assuming a semirigid C_{2v} structure for the ground state $\text{oH}_2\text{-H}_2\text{O}$ complex in the solid (*i.e.* $\zeta \approx 1$), we can qualitatively understand the $\text{oH}_2\text{-H}_2\text{O}$ complex features in the ν_2 and ν_3 regions as parallel and perpendicular bands, respectively, of an asymmetric top near the prolate symmetric top limit (54). In this description the C_2 symmetry axis now coincides with the least moment of inertia and is relabeled as the A axis, while rotations about the new B and C axes are rendered infeasible by the matrix surroundings. Thus, the rotational constant for the complex around the C_2 symmetry axis should be comparable to the B constant of the water monomer, $A_{\text{oH}_2\text{-H}_2\text{O}} \approx B_{\text{H}_2\text{O}}$, and the new B and C rotational constants for the complex are effectively zero. The rotational term energies for the symmetric top are given by (54):

$$E(J,K) = BJ(J+1) + (A-B)K^2 \quad \rightarrow AK^2 \quad \text{as } B \rightarrow 0 \quad [9].$$

Thus, we see that the features bunching near the ν_2 H_2O band origin arise from the $\Delta K = 0$ selection rule for parallel bands which causes the $\text{oH}_2\text{-pH}_2\text{O}$ and $\text{oH}_2\text{-oH}_2\text{O}$ peaks to overlap, while the more widely separated $\text{oH}_2\text{-pH}_2\text{O}$ and $\text{oH}_2\text{-oH}_2\text{O}$ features in the ν_3 H_2O region arise from the $\Delta K = \pm 1$ selection rule for perpendicular bands.

With this insight we can revisit the analysis of "vibrationally averaged rotational constants" presented above in Eqs. [4] and [5] for the water monomers, and apply it to the main oH_2 -water complex peaks straddling the ν_3 H_2O and ν_3 D_2O band origins. Using symmetric top quantum numbers (J,K) we assign the oH_2 -water complex peaks just to the blue of the $0_{00} \leftarrow 1_{01}$ water monomer transitions as $(0,0) \leftarrow (1,1)$, and those just to the red of the $1_{01} \leftarrow 0_{00}$ monomer transition as $(1,1) \leftarrow (0,0)$. We note that the relabeling of the rotational axes spoils the expected correlation between the free rotor Ka and the symmetric top K quantum numbers. We define another energy difference:

$$\Delta E_{\text{sym}} \equiv \bar{\nu} [(1,1) \leftarrow (0,0)] - \bar{\nu} [(0,0) \leftarrow (1,1)] \quad [10]$$

where $\bar{\nu}$ again signifies the transition wavenumber. From Eq. [9] we can relate this energy difference to the A rotational constants of the oH_2 -water complex in the ground and excited

vibrational states:

$$\Delta E_{\text{sym}} = (A)_{v=1} + (A)_{v=0} = 2(A)_{\text{avg}} \quad [11].$$

From the data in Tables 1 and 2 we find $A_{\text{avg}}(\nu_3 \text{ oH}_2\text{-H}_2\text{O}) = 16.5 \text{ cm}^{-1}$ as compared with the monomer $B_{\text{avg}}(\text{H}_2\text{O}) \approx 14.5 \text{ cm}^{-1}$, and $A_{\text{avg}}(\nu_3 \text{ oH}_2\text{-D}_2\text{O}) = 8.0 \text{ cm}^{-1}$ as compared with the monomer $B_{\text{avg}}(\text{D}_2\text{O}) \approx 7.3 \text{ cm}^{-1}$. The reduction of the I_A moment of inertia in the complex relative to I_B for the water monomers is a consequence of the semi-rigid nature of the complex; the H(D) atoms are not always fully extended away from the C_2 symmetry axis. We judge this level of (dis)agreement as acceptable, given the crude nature of our model.

The small ($\sim 0.1 \text{ cm}^{-1}$) splittings in these oH₂-water complex features observed in annealed samples are probably due to a combination of the oH₂ molecules occupying in-plane (ip) and out-of-plane (oop) positions relative to the H₂O subunit in the hcp pH₂ lattice (15), and to lifting of the M-degeneracy of the symmetric top rotational levels by the crystal field. A more detailed assignment of these splittings, and of the minor features attributed to oH₂-water complexes in the Tables, will require quantitative modeling of the cage effect, and the partial cancellation and pure crystal field terms in Eq. [7].

We can qualitatively explain the spectral shifts of the other (oH₂)_n-H₂O cluster features in the ν_3 region by a simple electrostatic argument. The strength of the binding between oH₂ and H₂O molecules depends on the degree of mutual orientation between the oH₂ and H₂O subunits, which increases with the H₂O subunit angular momentum. Thus, the features in the 3725 to 3735 cm^{-1} region are due to (oH₂)_n-oH₂O clusters, and these absorptions are blue shifted due to electrostatic stabilization of the $J = 1, v = 0$ initial level. Conversely, those in the 3745 to 3760 cm^{-1} region are due to (oH₂)_n-pH₂O clusters, and these absorptions are red shifted due to stabilization of the $J = 1, v = 1$ final level.

G. Nuclear Spin Conversion in oH₂-water Complexes and (oH₂)_n-water Clusters

Surprisingly, NSC of metastable oH₂O or pD₂O molecules is not accelerated appreciably by complexation with a single oH₂ molecule. This argues against the importance of pairwise magnetic dipole-dipole interactions in the water NSC process, which illuminates the observed independence of the rate of NSC for CH₄ in solid pH₂ for oH₂ concentrations below 2 % (19). A

correlation plot of the integrated intensities of the $0_{00} \leftarrow 1_{01} \nu_3$ H₂O monomer peak at 3719.79 cm⁻¹ and of the $(0,0) \leftarrow (1,1)$ oH₂-oH₂O complex peak at 3725.46 cm⁻¹ shows a strong linear correlation ($r^2 = 0.994$) over the two hour duration of the experiment depicted in FIG. 6. Furthermore, the decay of the $(0,0) \leftarrow (1,1)$ oH₂-oH₂O peak at 3725.46 cm⁻¹ is matched by the growth of the $(1,1) \leftarrow (0,0)$ oH₂-pH₂O peak at 3758.46 cm⁻¹; the sum of the integrated intensities of these two features decays slowly by about 10 % per hour, matching the slow decay of the overlapped oH₂-oH₂O and oH₂-pH₂O peaks in the 1593 to 1595 cm⁻¹ section of the ν_2 H₂O region. This suggests that oH₂-oH₂O complexes convert directly into oH₂-pH₂O complexes, and that absorption features for both species have nearly the same transition strength. We suppose that the 10 % per hour decrease in total oH₂-H₂O intensity is due to NSC of oH₂ complexed with H₂O.

Even more surprising is the observation that the integrated intensity of the bunch of (oH₂)_n-oH₂O cluster features in the 3725 to 3735 cm⁻¹ region shown in FIG. 12(b) decays *more slowly* than do the oH₂O monomer absorptions! This is just the opposite of what we expected after learning of the increased rate of NSC for CH₄ in solid pH₂ for oH₂ concentrations above 10 % (19). Unfortunately, we did not investigate the kinetics of this process in detail; however, the integrated intensity of the (oH₂)_n-oH₂O cluster features in FIG. 12(b) decreased by only 50 % after the first hour, and by only 70 % after five hours. We speculate that somehow the NSC processes for the oH₂ and oH₂O species are linked, with the longer lived oH₂ species providing a "spin reservoir" to replenish the oH₂O population.

H. Dopant-Induced IR Activity and Cooperative Transitions

Dopant induced IR activity and dopant-host cooperative absorptions in RVD pH₂ solids containing neutral chemically interesting dopants have been reported and discussed previously (25,32-34,77). FIG. 13. shows the dependence of H₂O-induced IR activity on NSC of the H₂O dopant; the peak positions and assignments are summarized in Table 6. The sharp Q₁(0) H₂ transition at 4149.03 cm⁻¹ induced by pH₂O is characteristic of a spherically symmetric J = 0 perturber, in which case the only possible induction mechanism is short range overlap interactions (32-34). The sharpness of this line indicates that dopant-host interactions have resulted in strong (several cm⁻¹) shifting of the vibrations of the nearby participating pH₂ molecules, detuning them from the delocalized vibron band of the solid (34). The broader, red-

degraded $Q_1(0)$ H_2 feature peaking near 4149.8 cm^{-1} induced by oH_2O is characteristic of a perturber possessing nonzero rotationally averaged electrostatic multipole moments, enabling long range dopant- pH_2 interactions. The asymmetric "vibron-hopping" lineshape is reminiscent of the familiar oH_2 electric-quadrupole-induced $Q_1(0)$ H_2 line near 4153.1 cm^{-1} (11,32-34).

Working from these origins, we see a number of cooperative transitions in which a pure H_2 vibrational transition is accompanied by a pure rotational transition of the dopant molecule. This has the net effect of "upshifting" the dopant's rotational spectrum from the far-IR to the mid-IR, although the rotational features observed in this manner are for a trapped water molecule additionally perturbed by the pH_2 vibrational excitation. The $1_{10} \leftarrow 1_{01}$ oH_2O rotational transition is the most strongly perturbed, showing an 18 % decrease from the gas phase; the same transition also shows the broadest linewidth in the ν_2 H_2O rovibrational band. Otherwise we see 2 to 5 % reductions of gas phase rotational spacings, and 2 to 3 cm^{-1} linewidths, all comparable to the values reported above in Tables 4 and 5 for the direct IR rovibrational Type B transitions; thus, rotational dephasing (as distinct from rovibrational dephasing) is the dominant linebroadening mechanism for all these transitions. All we can say at present about the weak features near 4140 cm^{-1} is that they are due to the presence of oH_2 - H_2O complexes.

FIG. 14. shows the dependence of D_2O -induced IR activity on NSC of the D_2O dopant, and also includes some HDO related features which remain constant for the duration of the experiment. All of these observations, and their consequences, are very similar to those for the H_2O dopant, allowing for the smaller rotational constants of HDO and D_2O . The HDO induced $Q_1(0)$ H_2 peak is probably overlapped by the corresponding D_2O features; we use 4149.0 cm^{-1} as the origin for calculating the HDO rotational energies in the cooperative transitions reported in Table 6. The small peak at 4153.25 cm^{-1} remains unassigned, but it is definitely distinguishable from the oH_2 induced $Q_1(0)$ line which peaks at 4153.10 cm^{-1} (2,7).

V. SUMMARY

Isolated H_2O , D_2O and HDO molecules exist as nearly free rotors in solid pH_2 , with rotational constants typically within a few percent of the gas phase values. The linewidths of H_2O transitions indicate that rovibrational dephasing of the upper states in Type B bands by dopant-host interactions is much faster than dephasing of the upper states in Type A bands by IVR. Lineshape changes upon annealing indicate that inhomogeneous broadening of the water

monomer transitions is of order 0.1 cm^{-1} in RVD pH_2 solids. The gas-to-matrix red shifts of the water monomer rovibrational transitions increase monotonically with increasing excitation energy, but the details remain poorly understood. NSC of isolated oH_2O and pD_2O monomers follow first order kinetics, with single exponential decay lifetimes at $T = 2.4 \text{ K}$ of $1900 \pm 100 \text{ s}$, and $860 \pm 50 \text{ s}$, respectively.

Formation of oH_2 -water complexes, even at residual oH_2 concentrations of only 100 ppm, results in the appearance of a large number of additional absorption features. The main features of the $\text{oH}_2\text{-H}_2\text{O}$ and $\text{oH}_2\text{-D}_2\text{O}$ spectra are explained qualitatively by assuming a semi-rigid C_{2v} structure with the oH_2 acting as a proton donor to the O atom. NSC of oH_2 -water complexes proceeds at very nearly the same rate as for the corresponding water monomer, refuting the proposed role of pairwise magnetic dipole-dipole interactions between oH_2 and $J = 1$ water molecules in accelerating the NSC process. At elevated oH_2 concentrations of 1000 ppm, absorptions of larger $(\text{oH}_2)_n$ -water clusters are observed. Somehow oH_2O and pD_2O molecules clustered with several oH_2 molecules survive longer than the isolated $J = 1$ water monomers.

The presence of water dopants results in a number of dopant-induced IR absorption features of the pH_2 host, and in cooperative water- pH_2 transitions in which the vibrational excitation of the pH_2 solid is accompanied by a pure rotational transition of the water dopant. The linewidths of these pure rotational transitions match well with those for the direct IR Type B rovibrational transitions of the water dopants, indicating that rotational dephasing is the dominant linebroadening mechanism in both cases.

ACKNOWLEDGEMENTS

We thank Profs. D.T. Anderson, R.J. Hinde, and T. Momose for many valuable discussions on the spectroscopy of doped pH_2 solids which improved our understanding of the phenomena reported in this manuscript.

REFERENCES

1. R. Steinhoff, K.V.S.R. Apparao, D.W. Ferguson, K.N. Rao, B.P. Winnewisser, and M. Winnewisser, *Appl. Opt.* **32**, 6577-6581 (1993).
2. R. Steinhoff, K.V.S.R. Apparao, D.W. Ferguson, K.N. Rao, B.P. Winnewisser, and M. Winnewisser, *Can. J. Phys.* **72**, 1122-1136 (1994).

3. R. Steinhoff, B.P. Winnewisser, and M. Winnewisser,
Phys. Rev. Lett. **73**, 2833-2836 (1994).
4. M. Mengel, B.P. Winnewisser, and M. Winnewisser, *Phys. Rev. B* **55**, 10420-10433 (1997).
5. M. Mengel, B.P. Winnewisser, and M. Winnewisser,
J. Low Temp. Phys. **111**, 757-762 (1998).
6. M. Mengel, B.P. Winnewisser, and M. Winnewisser,
J. Mol. Spectrosc. **188**, 221-244 (1998).
7. H.P. Gush, W.F.J. Hare, E.J. Allin, and H.L. Welsh, *Can. J. Phys.* **38**, 176-193 (1960).
8. J. Van Kranendonk and G. Karl, *Rev. Mod. Phys.* **40**, 531-555 (1968).
9. R.D.G. Prasad, M.J. Clouter, and S.P. Reddy, *Phys. Rev. A* **17**, 1690-1694 (1978).
10. I.F. Silvera, *Rev. Mod. Phys.* **52**, 393-452 (1980).
11. J. Van Kranendonk, "Solid Hydrogen," Plenum, New York, 1983.
12. K.N. Rao, J.R. Gaines, T.K. Balasubramanian, and R. D'Cunha,
Acta Physica Hungarica **55**, 383-393 (1984).
13. G. Varghese, R.D.G. Prasad, and S. Paddi Reddy, *Phys Rev A* **35**, 701-707 (1987).
14. T. Oka, *Annu. Rev. Phys. Chem.* **44**, 299-333 (1993).
15. D.P. Weliky, K.E. Kerr, T.J. Byers, Y. Zhang, T. Momose, and T. Oka,
J. Chem. Phys. **105**, 4461-4481 (1996).
16. T. Momose, *J. Chem. Phys.* **107**, 7695-7706 (1997).
17. T. Momose and T. Shida, *Bull. Chem. Soc. Jpn.* **71**, 1-15 (1998).
18. Y. Zhang, T.J. Byers, M.C. Chan, T. Momose, K.E. Kerr, D.P. Weliky, and T. Oka,
Phys. Rev. B **58**, 218-233 (1998).
19. M. Miki and T. Momose,
Fiz. Nizk. Temp **26**, 899-908 (2000) [*Low Temp. Phys.* **26**, 661-668 (2000)].
20. M. Fushitani, T. Shida, T. Momose, and M. Rasanen,
J. Phys. Chem. A **104**, 3635-3641 (2000).
21. H. Katsuki and T. Momose, *Phys. Rev. Lett.* **84**, 3286-3289 (2000).
22. M.C. Chan, M. Okumura, and T. Oka, *J. Phys. Chem. A* **104**, 3775-3779 (2000).
23. H. Katsuki, T. Momose, and T. Shida, *J. Chem. Phys.* **116**, 8411-8417 (2002).
24. H. Katsuki, T. Nakamura, and T. Momose, *J. Chem. Phys.* **116**, 8881-8892 (2002).
25. M.E. Fajardo and S. Tam, *J. Chem. Phys.* **108**, 4237-4241 (1998).

26. S. Tam and M.E. Fajardo, *Rev. Sci. Instrum.* **70**, 1926-1932 (1999).
27. S. Tam, M.E. Fajardo, H. Katsuki, H. Hoshina, T. Wakabayashi, and T. Momose, *J. Chem. Phys.* **111**, 4191-4198 (1999).
28. M.E. Fajardo and S. Tam, *J. Chem. Phys.*, **115**, 6807-6810 (2001).
29. S. Tam and M.E. Fajardo, *Fiz. Nizk. Temp* **26**, 889-898 (2000) [*Low Temp. Phys.* **26**, 653-660 (2000)].
30. S. Tam, M. Macler, M.E. DeRose, and M.E. Fajardo, *J. Chem. Phys.* **113**, 9067-9078 (2000).
31. X. Wang, L. Andrews, S. Tam, M.E. DeRose, and M.E. Fajardo, *J. Am. Chem. Soc.* **125**, 9218-9228 (2003).
32. D.T. Anderson, R.J. Hinde, S. Tam, and M.E. Fajardo, *J. Chem. Phys.* **116**, 594-607 (2002).
33. R.J. Hinde, D.T. Anderson, S. Tam, and M.E. Fajardo, *Chem. Phys. Lett.* **356**, 355-360 (2002).
34. R.J. Hinde, *J. Chem. Phys.* **119**, 6-9 (2003).
35. M. Van Thiel, E.D. Becker, and G.C. Pimentel, *J. Chem. Phys.* **27**, 486-490 (1957).
36. E. Catalano and D.E. Milligan, *J. Chem. Phys.* **30**, 45-47 (1959).
37. J.A. Glasel, *J. Chem. Phys.* **33**, 252-255 (1960).
38. R.L. Redington and D.E. Milligan, *J. Chem. Phys.* **37**, 2162-2166 (1962).
39. R.L. Redington and D.E. Milligan, *J. Chem. Phys.* **39**, 1276-1284 (1963).
40. D.W. Robinson, *J. Chem. Phys.* **39**, 3430-3432 (1963).
41. H.P. Hopkins, Jr., R.F. Curl, Jr., and K.S. Pitzer, *J. Chem. Phys.* **48**, 2959-2865 (1968).
42. K.B. Harvey and H.F. Shurvell, *J. Mol. Spectrosc.* **25**, 120-122 (1968).
43. A.J. Tursi and E.R. Nixon, *J. Chem. Phys.* **52**, 1521-1528 (1970).
44. D.P. Strommen, D.M. Gruen, and R.L. McBeth, *J. Chem. Phys.* **58**, 4028-4029 (1973).
45. G.P. Ayers and A.D.E. Pullin, *Chem. Phys. Lett.* **29**, 609-615 (1976).
46. E.J. Murby and A.D.E. Pullin, *Aust. J. Chem.* **32**, 1167-1176 (1979).
47. R.M. Bentwood, A.J. Barnes, and W.J. Orville-Thomas, *J. Mol. Spectrosc.* **84**, 391-404 (1980).
48. H.A. Fry, L.H. Jones, and B.I. Swanson, *Chem. Phys. Lett.* **105**, 547-550 (1984).
49. L. Manceron, A. Loutellier, and J.P. Perchard, *Chem. Phys.* **92**, 75-89 (1985).
50. A. Engdahl and B. Nelander, *J. Mol. Struct.* **193**, 101-109 (1989).

51. D. Forney, M.E. Jacox, and W.E. Thompson, *J. Mol. Spectrosc.* **157**, 479-493 (1993).
52. M.J. Weida and D.J. Nesbitt, *J. Chem. Phys.* **110**, 156-167 (1999).
53. C.Kittel, "Introduction to Solid State Physics, 6th Ed.," Wiley, New York, 1986.
54. G. Herzberg, "Molecular Spectra and Molecular Structure II. Infrared and Raman Spectra of Polyatomic Molecules," Kreiger, Malabar, FL, 1991.
55. J.M. Hutson, *J. Chem. Phys.* **92**, 157-168 (1990).
56. H.W. Kroto, "Molecular Rotation Spectra," Dover, New York, 1992.
57. A.D. Bykov, V.S. Makarov, N.I. Moskalenko, O.V. Naumenko, O.N. Ulenikov, and O.V. Zotov, *J. Mol. Spectrosc.* **123**, 126-134 (1987).
58. P. Jensen, *J. Mol. Spectrosc.* **133**, 438-460 (1989).
59. L.S. Rothman, et al., *J. Quant. Spectrosc. Radiat. Transfer* **60**, 665-710 (1998).
60. R.A. Toth, *J. Mol. Spectrosc.* **195**, 73-97 (1999).
61. R.A. Toth, *J. Mol. Spectrosc.* **195**, 98-122 (1999).
62. S. He, O.N. Ulenikov, G.A. Onopenko, E.S. Bekhtereva, X. Wang, S. Hu, H. Lin, and Q. Zhu, *J. Mol. Spectrosc.* **200**, 34-39 (2000).
63. R. Rey and J.T. Hynes, *J. Chem. Phys.* **104**, 2356-2368 (1996).
64. J.C. Deak, S.T. Rhea, L.K. Iwaki, and D.D. Dlott, *J. Phys. Chem. A* **104**, 4866-4875 (2000).
65. S. Tam and M.E. Fajardo, *Appl. Spectrosc.* **55**, 1634-1644 (2001).
66. R.S. Mulliken, *Phys. Rev.* **36**, 611-629 (1930); we adopt the standard spectroscopic notation " $L_v(J)$ " for rovibrational transitions of H_2 molecules to vibrational level v , originating from $v = 0$ and rotational level J , with $L = Q, S$, and U for $\Delta J = 0, +2$, and $+4$, respectively.
67. P.R. Griffiths and J.A. de Haseth, "Fourier Transform Infrared Spectrometry," Wiley, New York, 1986.
68. D.J. Nesbitt and R.W. Field, *J. Phys. Chem.* **100**, 12735-12756 (1996).
69. T. Momose, 58th Ohio State University International Symposium on Molecular Spectroscopy, Paper WA02, 2003; unpublished.
70. R.F. Curl, Jr., J.V.V. Kasper, and K.S. Pitzer, *J. Chem. Phys.* **46**, 3220-3227 (1967).
71. P.L. Chapovsky, *Chem. Phys. Lett.* **254**, 1-5 (1996).
72. P.L. Chapovsky, *Physica A* **233**, 441-448 (1996).
73. A.J. Barnes, in "Vibrational Spectroscopy of Trapped Species" (H.E. Hallam, Ed.), pp. 133-178. Wiley, London, 1973.

74. S.L. Shostak, W.L. Ebenstein, and J.S. Muentner, *J. Chem. Phys.* **94**, 5875-5882 (1991).
75. S.L. Shostak and J.S. Muentner, *J. Chem. Phys.* **94**, 5883-5890 (1991).
76. V.I. Starikov and A.E. Protasevich, *J. Mol. Struct.* **646**, 81-88 (2003).
77. K. Yoshioka and D.T. Anderson, *J. Chem. Phys.* **119**, 4731-4742 (2003).
78. L. Pauling, *Phys. Rev.* **36**, 430-443 (1930).

Table 1. Absorptions of H₂O monomers and oH₂-H₂O complexes at T = 2.4 K in pH₂ solids containing ~ 100 ppm oH₂. Peak positions (FWHM) and energy differences given in cm⁻¹.

assignment	gas phase ^a	-----as-deposited-----		-----annealed-----	
		in pH ₂	ΔE(gas-pH ₂)	in pH ₂	ΔE(gas-pH ₂)
oH ₂ -H ₂ O		1593.7 mult.		1593.7 mult.	
oH ₂ -oH ₂ O		1606.78		n.o.	
oH ₂ -pH ₂ O		1608.50		1608.48	
v ₂ [1 ₁₀ ← 1 ₀₁]	1616.712	1612.0 (7.4)	4.7	n.o.	
v ₂ [1 ₁₁ ← 0 ₀₀]	1634.967	1631.6 (1.7)	3.4	1631.5 (1.6)	3.5
v ₂ [2 ₁₂ ← 1 ₀₁]	1653.267	1649.0 (3.0)	4.3	n.o.	
2v ₂ [1 ₁₁ ← 0 ₀₀]	3196.093	3190.7 w	5.4	3190.7 (1.5)	5.4
oH ₂ -H ₂ O		3645.4 mult.		3645.4 mult.	
v ₁ [1 ₁₀ ← 1 ₀₁]	3674.697	3660.5 (1.4)	14.2	n.o.	
v ₁ [1 ₁₁ ← 0 ₀₀]	3693.294	3681.2 (2.7)	12.1	3681.2 (2.2)	12.1
v ₁ [2 ₁₂ ← 1 ₀₁]	3711.103	3698.4 (3.1)	12.7	n.o.	
v ₃ [0 ₀₀ ← 1 ₀₁]	3732.135	3719.79 (0.24)	12.35	n.o.	
oH ₂ -oH ₂ O [0,0 ← 1,1]		3725.46		n.o.	
oH ₂ -oH ₂ O		3728.33		n.o.	
oH ₂ -pH ₂ O [1,1 ← 0,0]		3758.46		3758.44	
v ₃ [1 ₀₁ ← 0 ₀₀]	3779.493	3765.50 (0.23)	13.99	3765.47 (0.18)	14.02
oH ₂ -pH ₂ O		3773.44		3773.42	
v ₃ [2 ₀₂ ← 1 ₀₁]	3801.420	3787.1 (2.5)	14.32	n.o.	
v ₂ +v ₃ [0 ₀₀ ← 1 ₀₁]	5307.475	5292.83 (0.26)	14.65	n.o.	
oH ₂ -oH ₂ O [0,0 ← 1,1]		5299.2 w		n.o.	
oH ₂ -pH ₂ O [1,1 ← 0,0]		5332.3 w		5332.26	
v ₂ +v ₃ [1 ₀₁ ← 0 ₀₀]	5354.873	5338.58 (0.23)	16.29	5338.54 (0.14)	16.33
v ₂ +v ₃ [2 ₀₂ ← 1 ₀₁]	5376.945	5360.3 (2.0)	16.6	n.o.	
2v ₂ +v ₃ [0 ₀₀ ← 1 ₀₁]	6847.726	6831.20 (0.23)	16.53	n.o.	
2v ₂ +v ₃ [1 ₀₁ ← 0 ₀₀]	6895.148	6876.91 (0.27)	18.24	6876.91 (0.20)	18.24
v ₁ +v ₃ [0 ₀₀ ← 1 ₀₁]	7226.024	7203.4 (0.5)	22.6	n.o.	
v ₁ +v ₃ [1 ₀₁ ← 0 ₀₀]	7273.000	7248.69 (0.23)	24.31	7248.65 (0.12)	24.35
v ₁ +v ₃ [2 ₀₂ ← 1 ₀₁]	7294.136	7269.4 (2.2)	24.7	n.o.	

a = Refs. (58,59)

mult. = multiple peaks

n.o. = not observed

w = weak

Table 2. Absorptions of D₂O monomers and oH₂-D₂O complexes at T = 2.4 K in pH₂ solids containing ~ 100 ppm oH₂. Peak positions (FWHM) and energy differences given in cm⁻¹.

assignment	gas phase ^a	-----as-deposited-----		-----annealed-----	
		in pH ₂	ΔE(gas-pH ₂)	in pH ₂	ΔE(gas-pH ₂)
oH ₂ -D ₂ O		1177.4 mult.		1177.4 mult.	
v ₂ [1 ₁₀ ← 1 ₀₁]	1190.221	1188.10 (0.27)	2.12	1188.07 (0.16)	2.15
v ₂ [1 ₁₁ ← 0 ₀₀]	1199.793	1197.71 (0.7)	2.08	1197.70 (0.7)	2.09
v ₂ [2 ₁₂ ← 1 ₀₁]	1209.388	1207.1 (1.5)	2.3	n.o.	
2v ₂ [1 ₁₁ ← 0 ₀₀]	2359.689	2356.4 w	3.3	2356.4 w	3.3
oH ₂ -D ₂ O		2663.4 mult.		2663.4 mult.	
v ₁ [1 ₁₀ ← 1 ₀₁]	2681.894	2673.35 (0.22)	8.54	n.o.	
v ₁ [1 ₁₁ ← 0 ₀₀]	2691.606	2683.0 (1.1)	8.6	2682.9 (1.1)	8.7
v ₁ [2 ₁₂ ← 1 ₀₁]	2701.004	2692 w	9	n.o.	
v ₃ [0 ₀₀ ← 1 ₀₁]	2775.602	2765.93 (0.25)	9.67	2765.97 (0.10)	9.63
oH ₂ -pD ₂ O [0,0 ← 1,1]		2769.27		n.o.	
oH ₂ -pD ₂ O		2771.2 w		n.o.	
oH ₂ -oD ₂ O		2782.62		2782.59	
oH ₂ -oD ₂ O [1,1 ← 0,0]		2785.22		2785.05 ^t	
				2785.15 ^t	
				2785.29 ^t	
v ₃ [1 ₀₁ ← 0 ₀₀]	2799.759	2789.43 (0.22)	10.33	2789.39 (0.11)	10.37
oH ₂ -D ₂ O		2793.8 w		2793.8 w	
v ₃ [2 ₀₂ ← 1 ₀₁]	2811.214	2800.4 (1.6)	10.8	n.o.	
v ₂ +v ₃ [0 ₀₀ ← 1 ₀₁]	3943.896	3932.55 (0.38)	11.35	n.o.	
oH ₂ -oD ₂ O		3952.25		3952.10 ^t	
				3952.20 ^t	
				3952.33 ^t	
v ₂ +v ₃ [1 ₀₁ ← 0 ₀₀]	3968.069	3956.07 (0.24)	12.00	3956.02 (0.12)	12.05
v ₂ +v ₃ [2 ₀₂ ← 1 ₀₁]	3979.562	3966.8 w	12.8	n.o.	
v ₁ +v ₃ [1 ₀₁ ← 0 ₀₀]	5385.788	5367.73 (0.24)	18.06	5367.67 (0.14)	18.12

a = Refs. (57,61,62)

mult. = multiple peaks

n.o. = not observed

t = components of a triplet

w = weak

Table 3. Absorptions of HDO monomers and oH₂-HDO complexes at T = 2.4 K in pH₂ solids containing ~ 100 ppm oH₂. Peak positions (FWHM) and energy differences given in cm⁻¹.

assignment	gas phase ^a	-----as-deposited-----		-----annealed-----	
		in pH ₂	ΔE(gas-pH ₂)	in pH ₂	ΔE(gas-pH ₂)
v ₂ [0 ₀₀ ← 1 ₀₁] oH ₂ -HDO oH ₂ -HDO	1387.976	n.o. 1402.5 mult. 1413.28		1386.91 ^h (0.12) 1402.5 mult. 1413.20 ^d 1413.29 ^d	1.07
v ₂ [1 ₀₁ ← 0 ₀₀]	1419.041	1416.96 (0.27)	2.08	1416.92 (0.17)	2.12
v ₂ [1 ₁₁ ← 0 ₀₀]	1435.300	1432.5 (1.8)	2.8	1432.6 (1.5)	2.7
v ₂ [2 ₁₂ ← 1 ₀₁]	1447.997	n.o.		1445.0 ^h (1.4)	3.0
v ₁ [0 ₀₀ ← 1 ₀₁] oH ₂ -HDO oH ₂ -HDO	2708.172	n.o. 2714.90 2725.5 mult.		2700.25 ^h (0.08) 2714.90 2725.48 ^t 2725.51 ^t 2725.58 ^t	7.92
v ₁ [1 ₀₁ ← 0 ₀₀]	2738.914	2730.02 (0.15)	8.89	2729.995 ^d (0.03) 2730.085 ^d (0.02) w	8.919 8.829
2v ₂ [1 ₀₁ ← 0 ₀₀]	2797.610	2793.82 (0.26)	3.79	2793.79 (0.18)	3.82
2v ₂ [1 ₁₁ ← 0 ₀₀]	2816.214	2811.6 (1.2) w	4.6	2811.6 (1.2) w	4.6
v ₃ [0 ₀₀ ← 1 ₀₁] oH ₂ -HDO oH ₂ -HDO	3691.958	n.o. 3702.55 3705.5 mult.		3680.37 ^h (0.07) w 3702.55 3705.39 ^t 3705.44 ^t 3705.53 ^t	11.59
v ₃ [1 ₀₁ ← 0 ₀₀]	3722.886	3710.27 (0.23)	12.62	3710.23 (0.11)	12.66
v ₃ [1 ₁₁ ← 0 ₀₀]	3736.160	3723.1 (1.4)	13.1	3723.1 (1.4)	13.1
v ₂ +v ₃ [1 ₀₁ ← 0 ₀₀]	5105.027	5090.4 w	14.6		

a = Refs. (59,60)

d = component of doublet

h = hot band (T = 4.8 K)

mult. = multiple peaks

n.o. = not observed

t = component of triplet

w = weak

Table 4. Gas-phase vs. solid-pH₂ excited vibrational state rotational spacings and rotational constants sums. Energy differences and rotational constants given in cm⁻¹.

vibrational mode	rotational level splitting	rotational constants sum	gas phase ^a	solid pH ₂	pH ₂ /gas
v ₂ H ₂ O	2 ₁₂ - 1 ₁₀	4C	36.555	37.0	1.01
v ₁ H ₂ O	2 ₁₂ - 1 ₁₀	4C	36.406	37.9	1.04
v ₃ H ₂ O	2 ₀₂ - 0 ₀₀	4B + A + C	69.285	67.3	0.97
v ₂ +v ₃ H ₂ O	2 ₀₂ - 0 ₀₀	4B + A + C	69.470	67.5	0.97
v ₁ +v ₃ H ₂ O	2 ₀₂ - 0 ₀₀	4B + A + C	68.112	66.0	0.97
v ₂ D ₂ O	2 ₁₂ - 1 ₁₀	4C	19.167	19.0	0.99
v ₁ D ₂ O	2 ₁₂ - 1 ₁₀	4C	19.110	18.7	0.98
v ₃ D ₂ O	2 ₀₂ - 0 ₀₀	4B + A + C	35.612	34.5	0.97
v ₂ +v ₃ D ₂ O	2 ₀₂ - 0 ₀₀	4B + A + C	35.666	34.2	0.96
v ₂ HDO	2 ₁₂ - 0 ₀₀	4C + A + B	60.021	58.1	0.97
v ₂ HDO	1 ₁₁ - 1 ₀₁	A - B	16.259	15.5	0.95
2v ₂ HDO	1 ₁₁ - 1 ₀₁	A - B	18.604	17.8	0.96
v ₃ HDO	1 ₁₁ - 1 ₀₁	A - B	13.274	12.8	0.96

a = Refs. (57,61,62)

Table 5. Gas-phase vs. solid-pH₂ vibrationally averaged rotational constants; ΔE_{asym} defined in Eq. [4].

transition	ΔE _{asym} (gas) (cm ⁻¹) ^a	ΔE _{asym} (pH ₂) (cm ⁻¹)	ΔE(pH ₂)/ΔE(gas)
v ₃ H ₂ O	47.358	45.71	0.965
v ₂ +v ₃ H ₂ O	47.398	45.75	0.965
2v ₂ +v ₃ H ₂ O	47.422	45.71	0.964
v ₃ D ₂ O	24.157	23.50	0.973
v ₂ +v ₃ D ₂ O	24.173	23.52	0.973
v ₁ HDO	30.742	29.79	0.969
v ₃ HDO	30.928	29.86	0.966

a = Refs. (gas1,5,6)

Table 6. Dopant-induced and cooperative absorptions in as-deposited pH₂ solids at T = 2.4 K. Peak positions (FWHM) and energy differences given in cm⁻¹.

assignment	in pH ₂	$\Delta E(\text{rot})$	gas phase ^a	$\Delta E/E_{\text{gas}}$
oH ₂ -oH ₂ O	4139.41 (0.03)			
oH ₂ -pH ₂ O	4139.65 (0.05)			
Q ₁ (0) H ₂ {pH ₂ O}	4149.03 (0.03)			
Q ₁ (0) H ₂ {oH ₂ O}	4149.67 (0.1)			
Q ₁ (0) H ₂ {oH ₂ O}	4149.81 (0.1)			
+ [1 ₁₀ ← 1 ₀₁] oH ₂ O	4164.9 (1.3)	15.2	18.578	0.818
+ [1 ₁₁ ← 0 ₀₀] pH ₂ O	4185.2 (2.4)	36.2	37.137	0.975
+ [2 ₁₂ ← 1 ₀₁] oH ₂ O	4203 (3)	53	55.702	0.95
+ [2 ₀₂ ← 0 ₀₀] pH ₂ O	4217.5 (2.5)	68.5	70.091	0.977
oH ₂ -D ₂ O	4139.13 (0.08)			
oH ₂ -D ₂ O	4139.35 (0.07)			
oH ₂ -D ₂ O	4139.60 (0.07)			
Q ₁ (0) H ₂ {oD ₂ O}	4148.97 (0.03)			
Q ₁ (0) H ₂ {pD ₂ O}	4149.61 (0.1)			
Q ₁ (0) H ₂ {pD ₂ O}	4149.76 (0.2)			
?	4153.25 (0.2)			
+ [1 ₁₀ ← 1 ₀₁] pD ₂ O	4159.35 (0.2)	9.7	10.567	0.92
+ [1 ₁₁ ← 0 ₀₀] oD ₂ O	4169.03 (0.9)	20.06	20.259	0.990
+ [2 ₁₂ ← 1 ₀₁] pD ₂ O	4178.2 (1.7)	28.5	29.952	0.95
+ [2 ₀₂ ← 0 ₀₀] oD ₂ O	4184.1 (1.5)	35.1	35.878	0.98
+ [1 ₀₁ ← 0 ₀₀] HDO	4164.5 (0.5)	15.5	15.508	1.00
+ [1 ₁₁ ← 0 ₀₀] HDO	4178.4 (1)	29.4	29.809	0.99

a = Refs. (57,61,62)

FIGURE CAPTIONS

FIG. 1. Energy levels and allowed rovibrational transitions for H_2O and D_2O molecules; adapted from Refs. (37,54). Type A bands have Δv_3 odd, *e.g.*: v_3 , v_2+v_3 , $2v_2+v_3$, v_1+v_3 . Type B bands have Δv_3 even, *e.g.*: v_1 , v_2 .

FIG. 2. IR absorption spectra (v_2 H_2O region) showing the effects of $\text{oH}_2\text{O} \rightarrow \text{pH}_2\text{O}$ conversion. The 0.7-mm-thick 30 ppm $\text{H}_2\text{O}/\text{pH}_2$ sample was deposited at $T = 2.4$ K over a 15 minute period. Trace (a) is for the 11-minute-old sample at $T = 2.4$ K; trace (b) is for the 42-minute-old sample at $T = 2.4$ K; trace (c) is for the 71-minute-old sample at $T = 2.4$ K; trace (d) is for the 272-minute-old sample at $T = 2.4$ K, after annealing at $T = 4.8$ K for 10 minutes. Each spectrum includes 20 co-added scans acquired over a 2.0 minute period (centered at the times given above), and is presented at 0.1 cm^{-1} resolution. Features marked "o" are stronger in samples deliberately doped with higher oH_2 concentrations, features marked "*" are coincident with atmospheric water vapor absorptions.

FIG. 3. IR absorption spectra (v_3 H_2O region) showing the effects of $\text{oH}_2\text{O} \rightarrow \text{pH}_2\text{O}$ conversion for the sample described in FIG. 2. Trace (a) is for the 6-minute-old sample at $T = 2.4$ K; trace (b) is for the 36-minute-old sample at $T = 2.4$ K; trace (c) is for the 66-minute-old sample at $T = 2.4$ K; trace (d) is for the 260-minute-old sample at $T = 2.4$ K, after annealing at $T = 4.8$ K for 10 minutes. Each spectrum includes 10 co-added scans acquired over a 2.0 minute period (centered at the times given above), and is presented at 0.05 cm^{-1} resolution. Features marked "o" are stronger in samples deliberately doped with higher oH_2 concentrations, features marked "*" are coincident with atmospheric water vapor absorptions, the feature marked "i" is due to a different water isotopomer (HDO).

FIG. 4. IR absorption spectra (v_2 D_2O region) showing the effects of $\text{pD}_2\text{O} \rightarrow \text{oD}_2\text{O}$ conversion. The 0.6-mm-thick 30 ppm $\text{D}_2\text{O}/\text{pH}_2$ sample was deposited at $T = 2.4$ K over a 10 minute period. Trace (a) is for the 1-minute-old sample at $T = 2.4$ K; trace (b) is for the 16-minute-old sample at $T = 2.4$ K; trace (c) is for the 31-minute-old sample at $T = 2.4$ K; trace (d) is for the 185-minute-old sample at $T = 2.4$ K, after annealing at $T = 4.8$ K for 20 minutes. Each spectrum includes 20

co-added scans acquired over a 2.0 minute period (centered at the times given above), and is presented at 0.1 cm^{-1} resolution. Features marked "o" are stronger in samples deliberately doped with higher oH_2 concentrations.

FIG. 5. IR absorption spectra ($\nu_3 \text{ D}_2\text{O}$ region) showing the effects of $\text{pD}_2\text{O} \rightarrow \text{oD}_2\text{O}$ conversion for the sample described in FIG. 4. Trace (a) is for the 6-minute-old sample at $T = 2.4 \text{ K}$; trace (b) is for the 36-minute-old sample at $T = 2.4 \text{ K}$; trace (c) is for the 192-minute-old sample at $T = 2.4 \text{ K}$, after annealing at $T = 4.8 \text{ K}$ for 20 minutes. Each spectrum includes 10 co-added scans acquired over a 2.0 minute period (centered at the times given above), and is presented at 0.05 cm^{-1} resolution. Features marked "o" are stronger in samples deliberately doped with higher oH_2 concentrations.

FIG. 6. Kinetics of $\text{oH}_2\text{O} \rightarrow \text{pH}_2\text{O}$ and $\text{pD}_2\text{O} \rightarrow \text{oD}_2\text{O}$ conversion at $T = 2.4 \text{ K}$. The solid lines are single exponential fits to the decay of the $J=1$ water species.

FIG. 7. IR absorption spectra ($\nu_2 \text{ HDO}$ region) showing the effects of temperature cycling. The 1.8-mm-thick $\text{H}_2\text{O}/\text{HDO}/\text{D}_2\text{O}/\text{pH}_2$ sample containing 5 ppm HDO was deposited at $T = 2.4 \text{ K}$. In sequence: trace (a) $T = 2.4 \text{ K}$; trace (b) $T = 4.8 \text{ K}$; trace (c) $T = 2.4 \text{ K}$; trace (d) $T = 4.8 \text{ K}$; trace (e) $T = 2.4 \text{ K}$. Each spectrum is presented at 0.01 cm^{-1} resolution. Features marked "o" are stronger in samples deliberately doped with higher oH_2 concentrations.

FIG. 8. IR absorption spectra ($\nu_3 \text{ HDO}$ region) showing the effects of temperature cycling for the sample described in FIG. 7. In sequence: trace (a) $T = 2.4 \text{ K}$; trace (b) $T = 4.8 \text{ K}$; trace (c) $T = 2.4 \text{ K}$; trace (d) $T = 4.8 \text{ K}$; trace (e) $T = 2.4 \text{ K}$. Each spectrum is presented at 0.01 cm^{-1} resolution. Features marked "o" are stronger in samples deliberately doped with higher oH_2 concentrations; the features marked "i" are due to a different water isotopomer (H_2O).

FIG. 9. IR absorption spectra ($\nu_1 \text{ HDO}$ region detail) showing the effects of temperature cycling. The 1.5-mm-thick $\text{D}_2\text{O}/\text{HDO}/\text{pH}_2$ sample containing 1 ppm HDO was deposited at $T = 2.4 \text{ K}$. In sequence: trace (a) $T = 2.4 \text{ K}$; trace (b) $T = 4.8 \text{ K}$; trace (c) $T = 2.4 \text{ K}$. Each spectrum is presented at 0.01 cm^{-1} resolution.

FIG. 10. Gas-to-matrix peak shifts for rovibrational transitions of water monomers in solid pH₂ at T=2.4 K. Data for as-deposited peak positions listed in Tables 1, 2 and 3. Points for transitions involving ν_2 excitation are circled.

FIG. 11. IR absorption spectra (ν_2 H₂O origin) showing the effects of oH₂/H₂O clustering. Trace (a) is for an as-deposited 1.0-mm-thick 10 ppm H₂O/pH₂ sample containing ≈ 100 ppm oH₂ at T = 2.4 K. Trace (b) is for an as-deposited 3.3-mm-thick 10 ppm H₂O/pH₂ sample containing ≈ 1000 ppm oH₂ at T = 2.4 K. Each spectrum is presented at 0.01 cm^{-1} resolution.

FIG. 12. IR absorption spectra (ν_3 H₂O region) showing the effects of oH₂/H₂O clustering. Trace (a) is the same data shown above in FIG. 3(a); this sample contains ≈ 100 ppm oH₂. Trace (b) is for the sample described above in FIG. 11(b); this sample contains ≈ 1000 ppm oH₂. Each spectrum is presented at 0.1 cm^{-1} resolution.

FIG. 13. IR absorption spectra (induced IR region) showing the effects of oH₂O \rightarrow pH₂O conversion for the sample described in FIG. 2. Traces (a), (b), and (c) are from the same spectra presented in FIG. 3 traces (a), (b), and (c). The labels " $Q_1(0) \text{ H}_2 \{X\}$ " are for pure $\Delta v = +1$ vibrational transitions of pH₂ induced by species X. The labels " $+ [J'_{K_a'K_c'} \leftarrow J''_{K_a''K_c''}] Y$ " are shorthand for the $Q_1(0) \text{ H}_2 + [J'_{K_a'K_c'} \leftarrow J''_{K_a''K_c''}] Y$ cooperative absorptions in which the neighboring dopant species Y undergoes a pure rotational transition.

FIG. 14. IR absorption spectra (induced IR region) showing the effects of pD₂O \rightarrow oD₂O conversion for the sample described in FIG. 4. Traces (a) and (b) are from the same spectra presented in FIG. 5 traces (a) and (b). The spectroscopic labels are explained in FIG. 13.

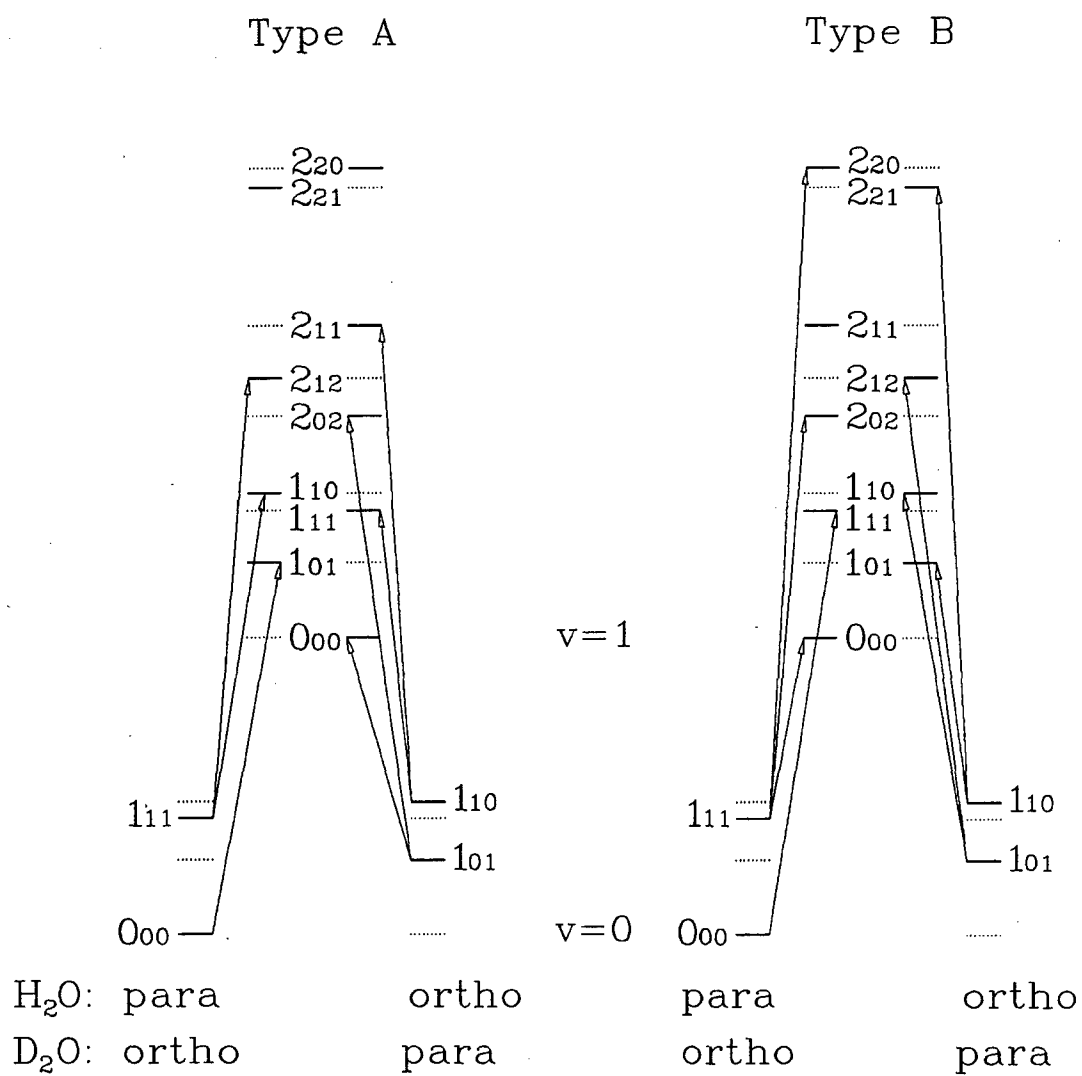


FIG. 1. Fajardo, Tam, and DeRose.

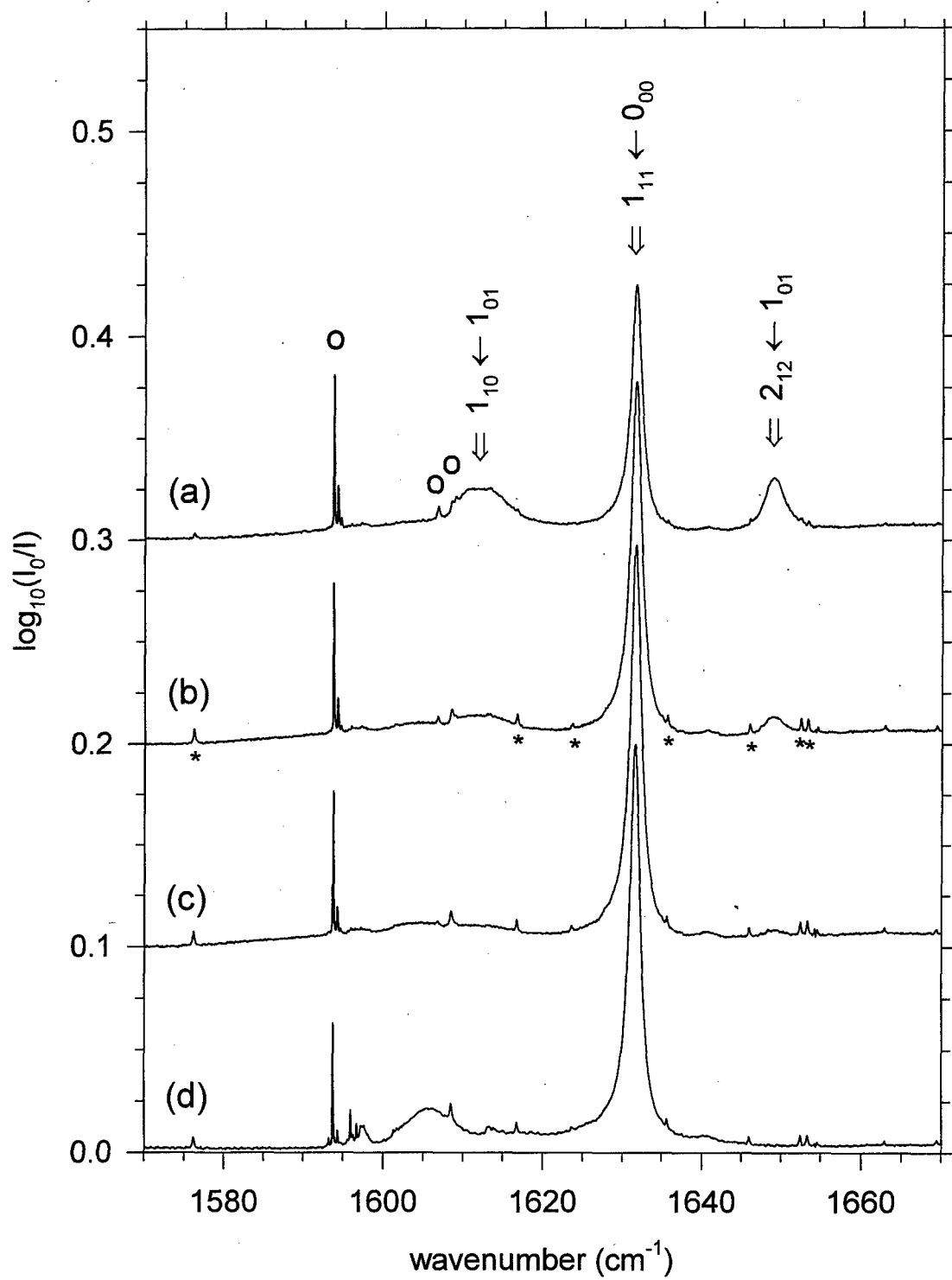


FIG. 2. Fajardo, Tam, and DeRose.

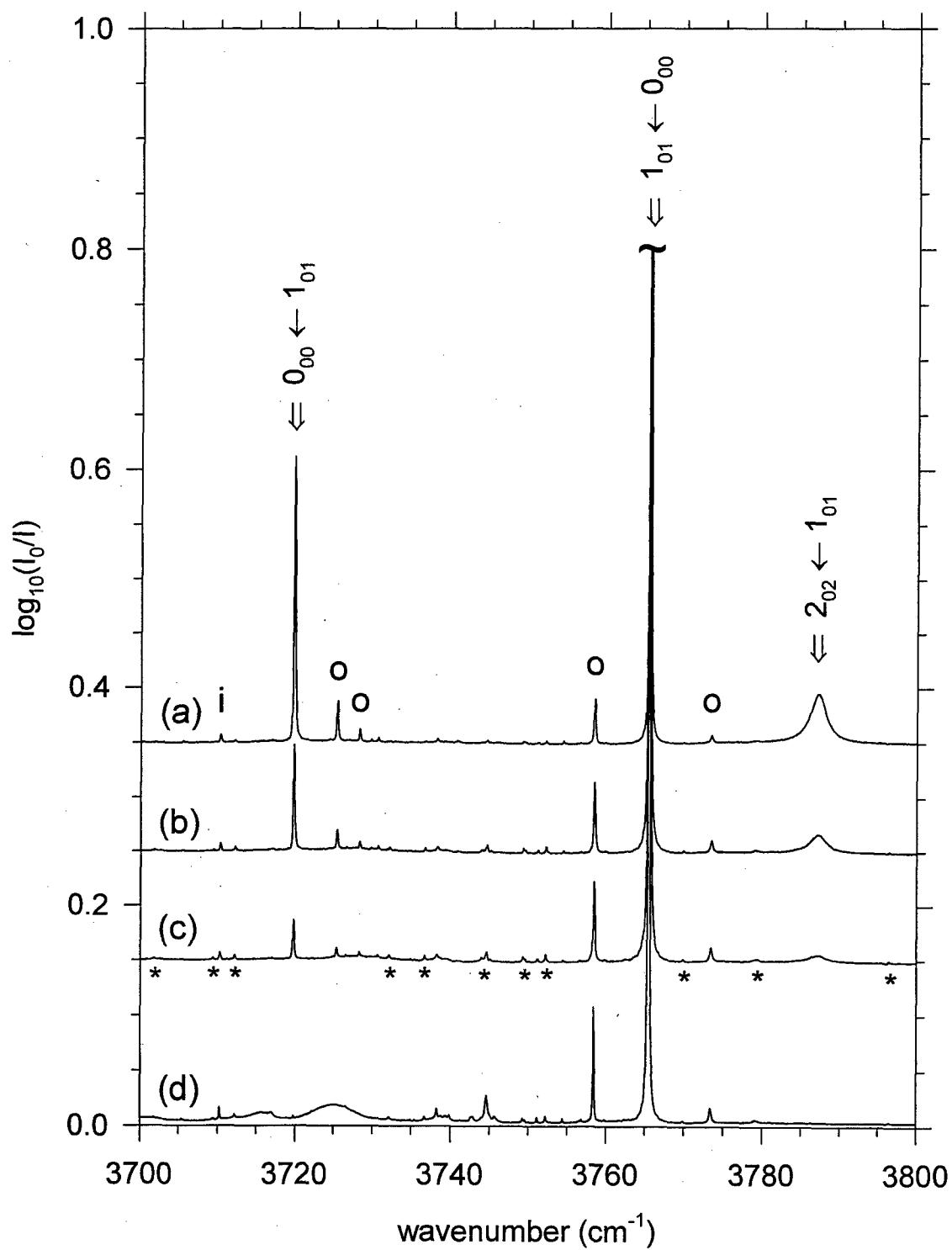


FIG. 3. Fajardo, Tam, and DeRose.

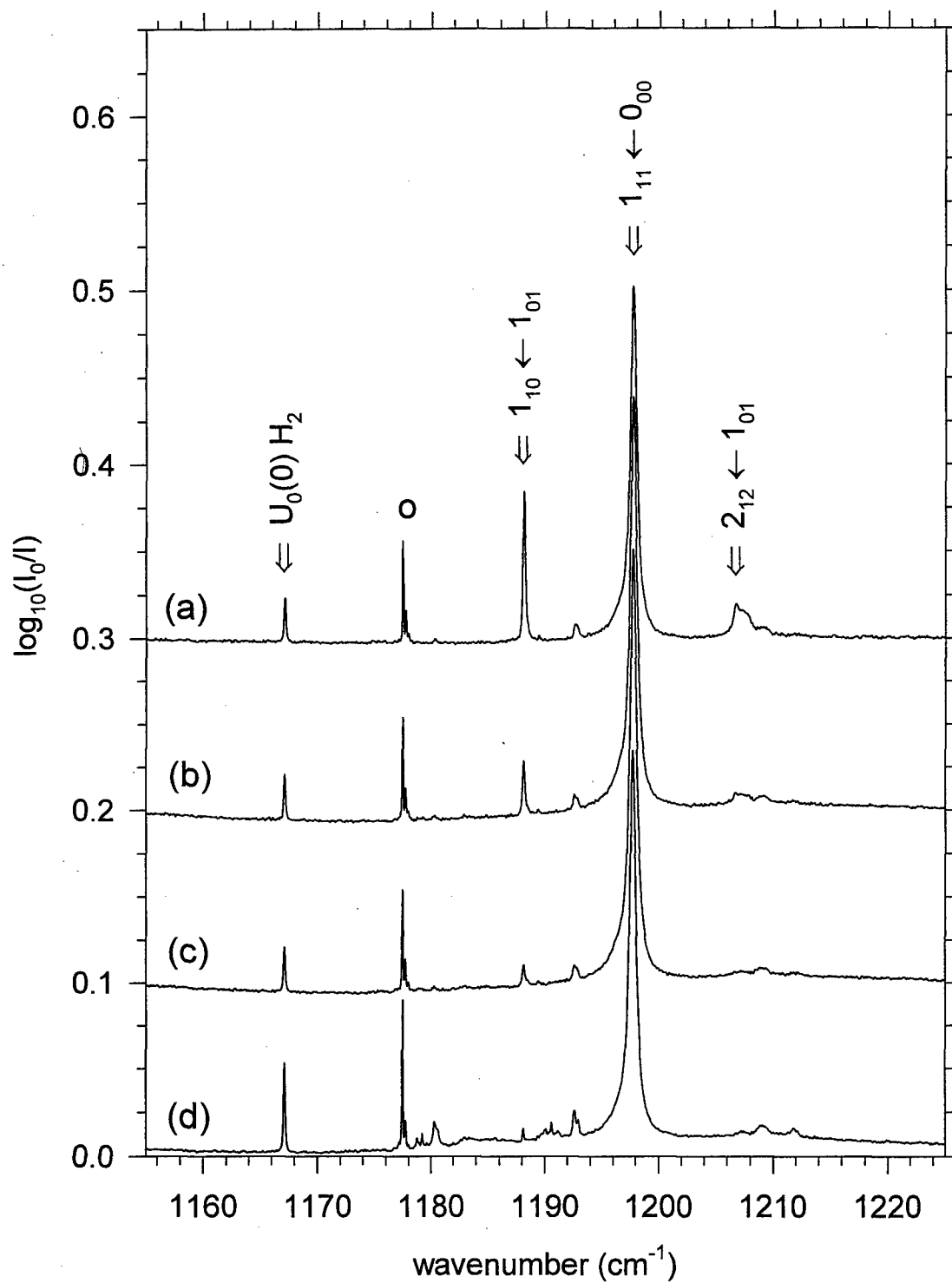


FIG. 4. Fajardo, Tam, and DeRose.

Approved for public release; distribution unlimited.

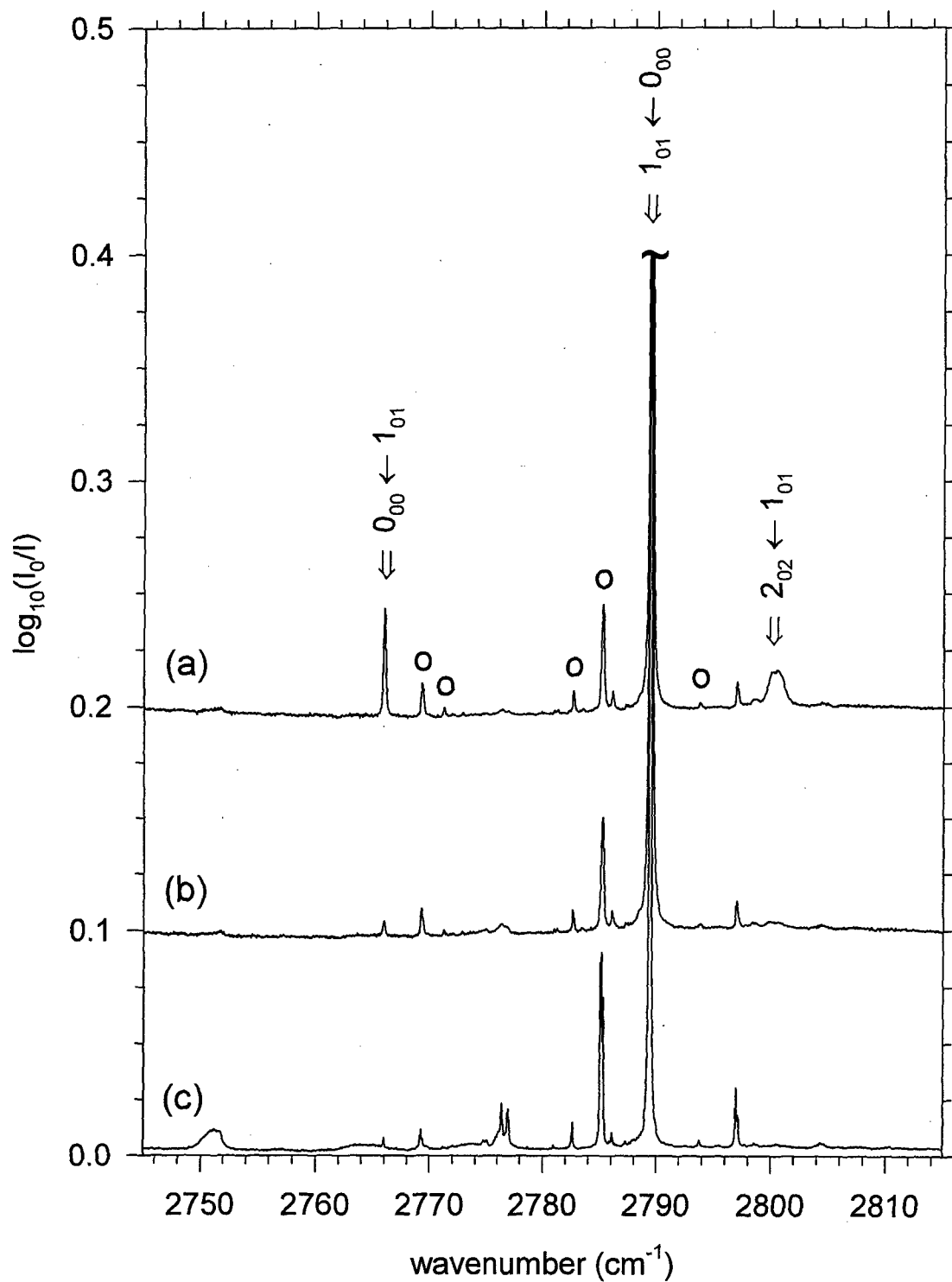


FIG. 5. Fajardo, Tam, and DeRose.

Approved for public release; distribution unlimited.

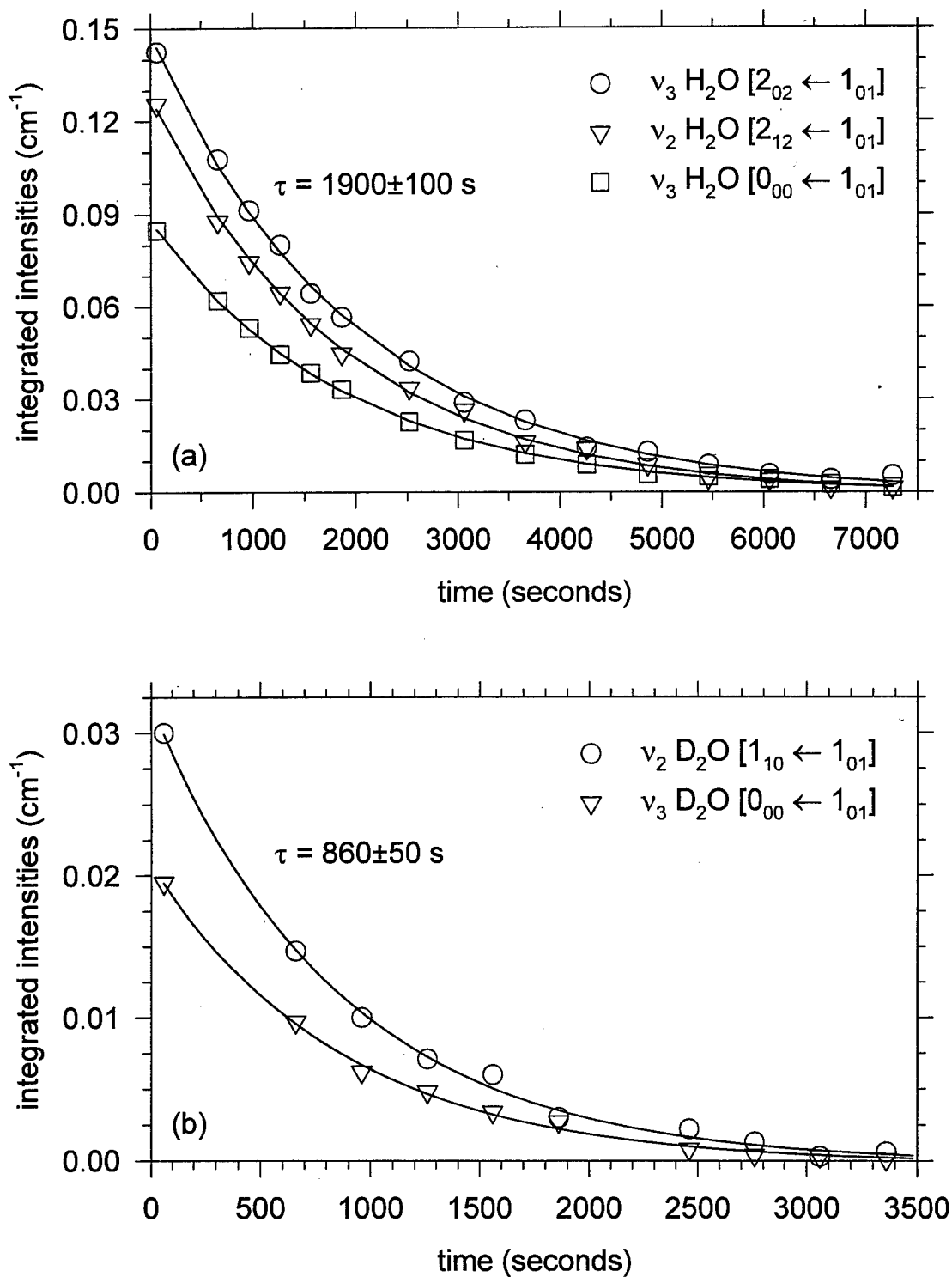


FIG. 6. Fajardo, Tam, and DeRose.

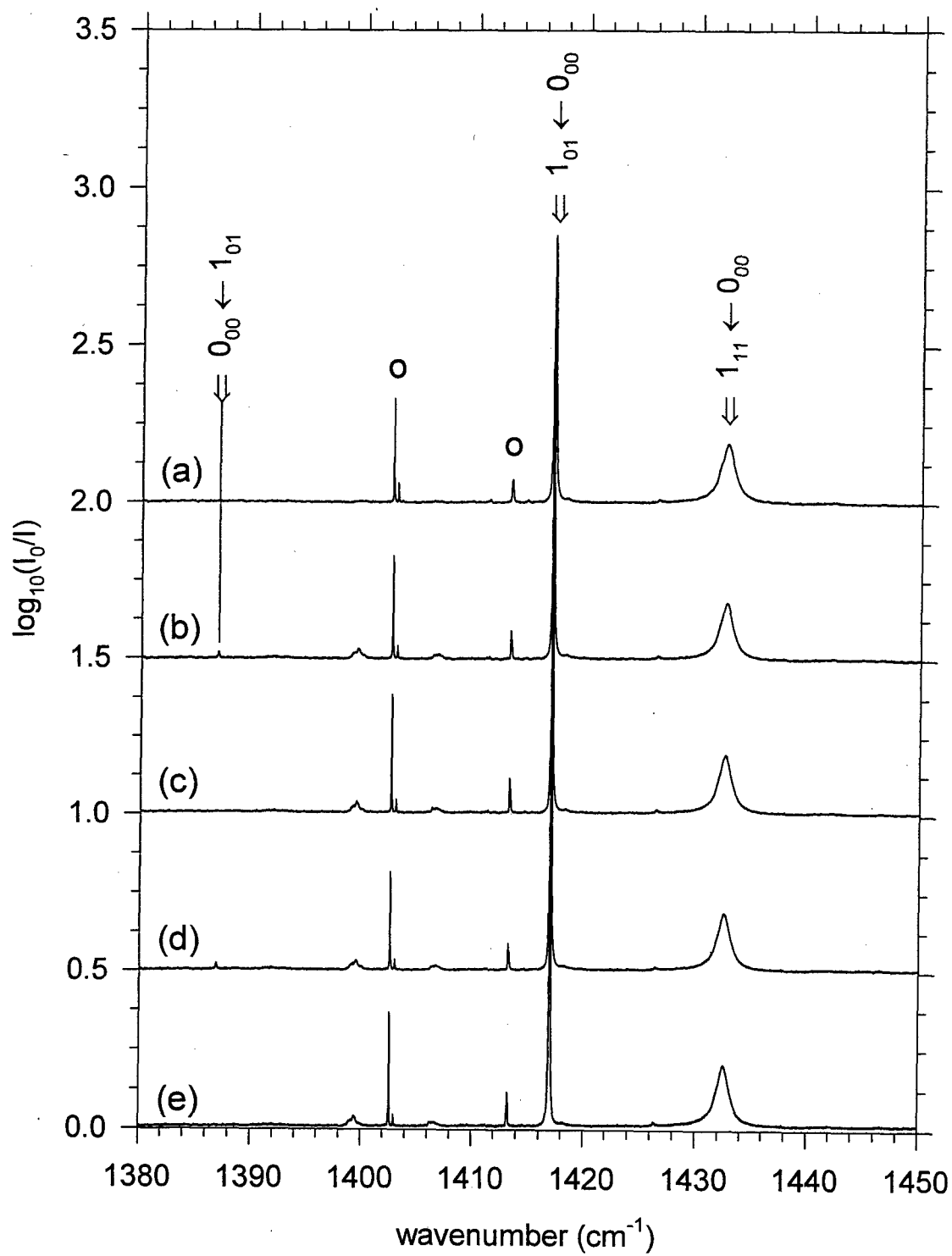


FIG. 7. Fajardo, Tam, and DeRose.

Approved for public release; distribution unlimited.

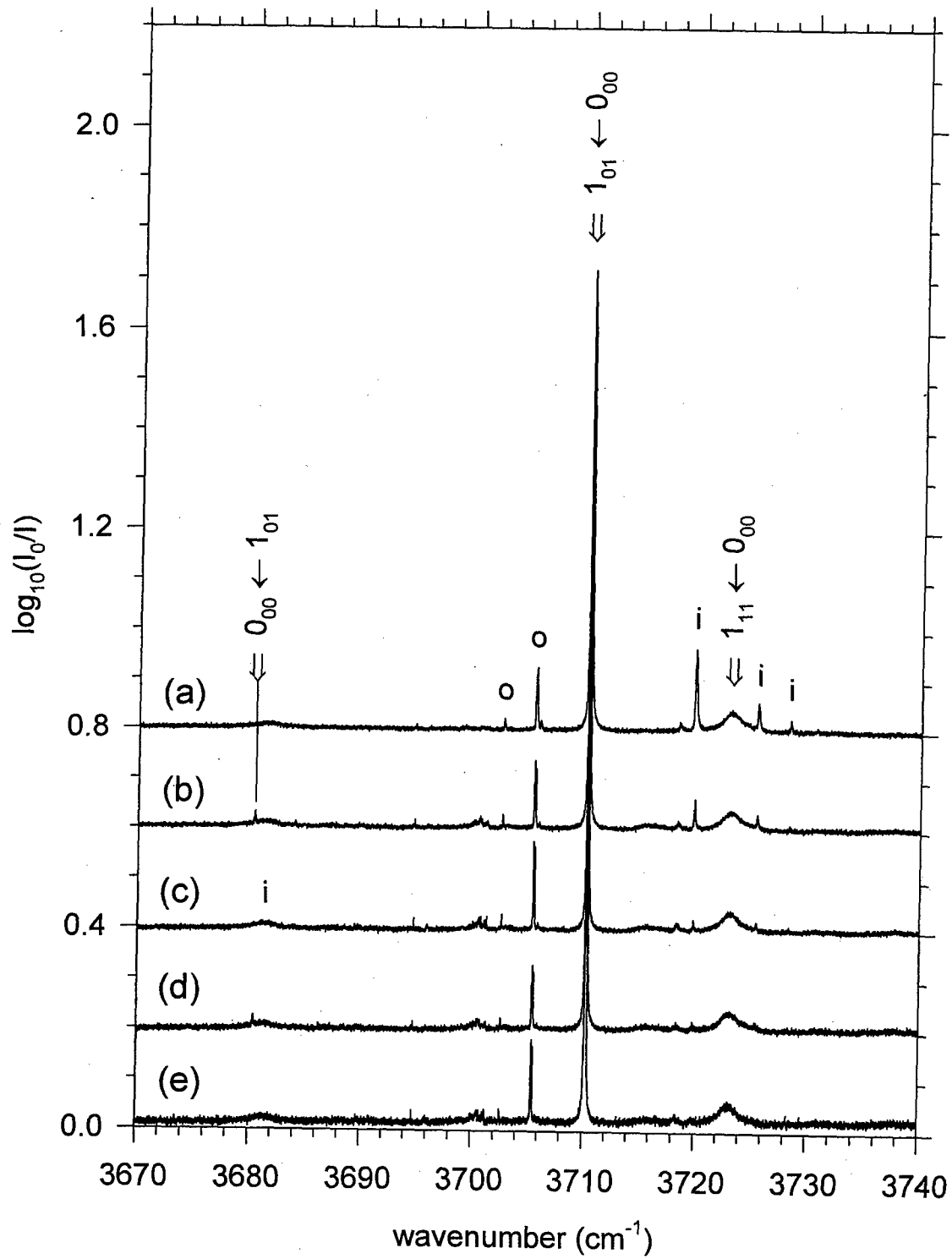


FIG. 8. Fajardo, Tam, and DeRose.

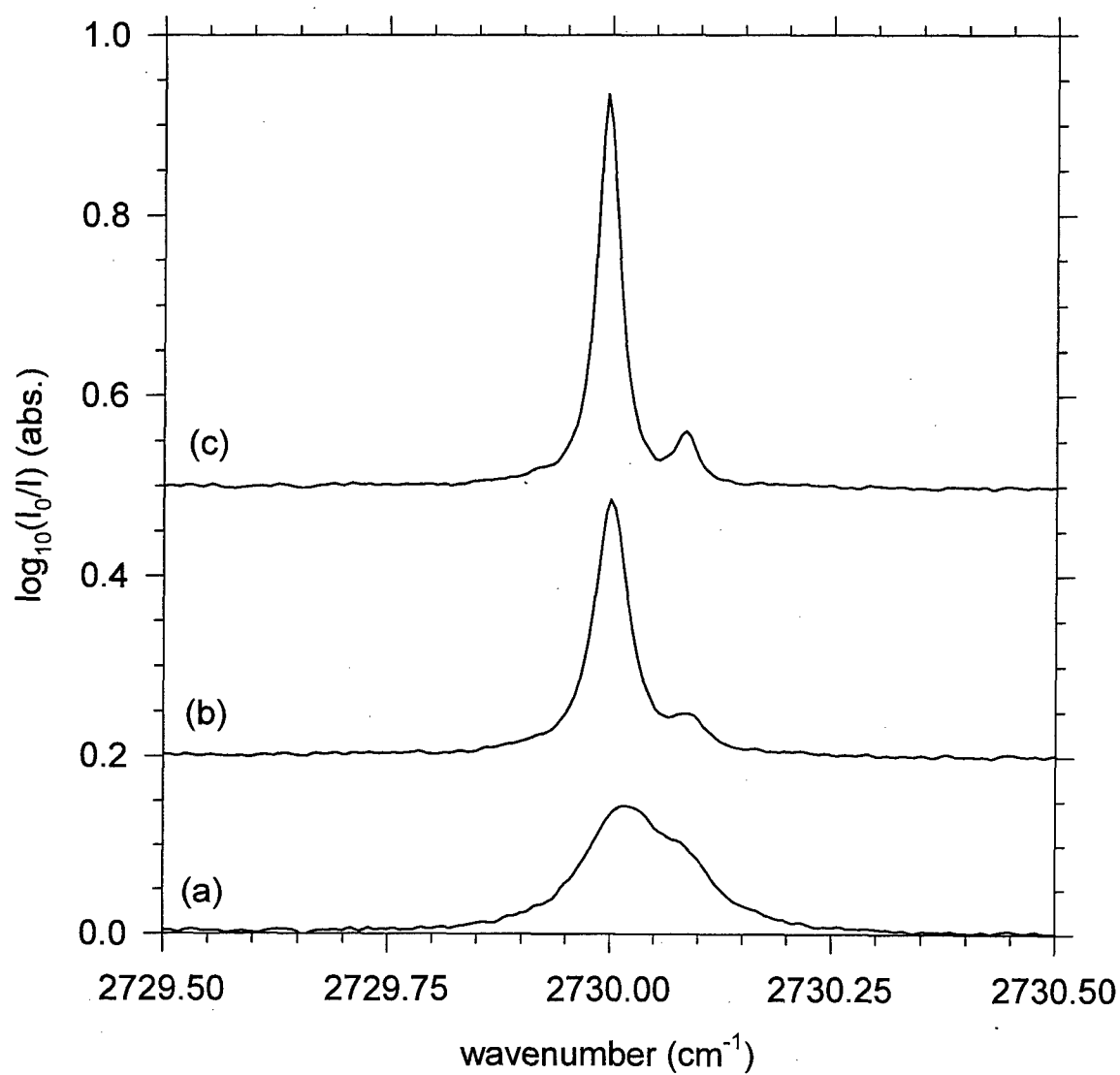


FIG. 9. Fajardo, Tam, and DeRose.

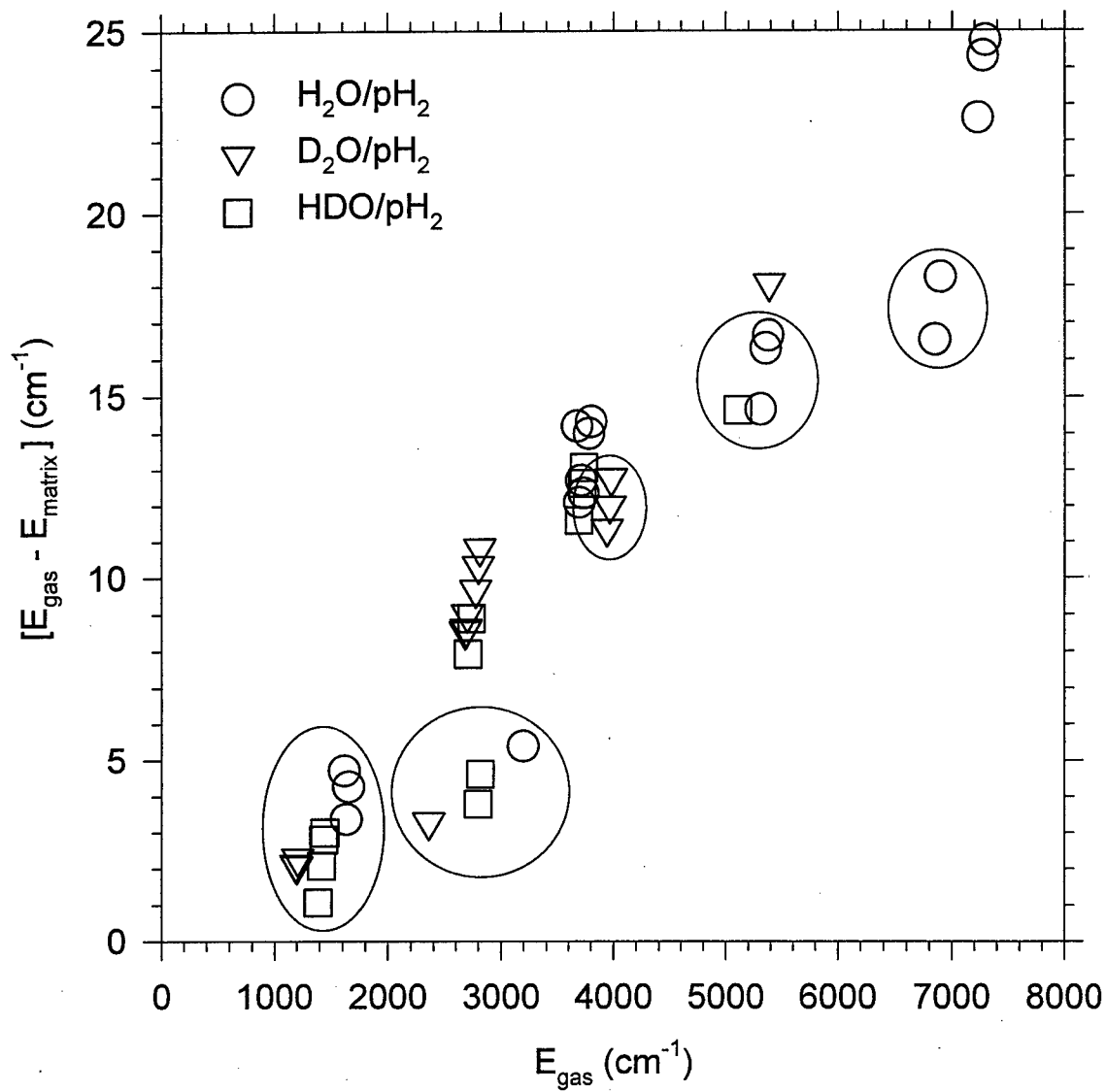


FIG. 10. Fajardo, Tam, and DeRose.

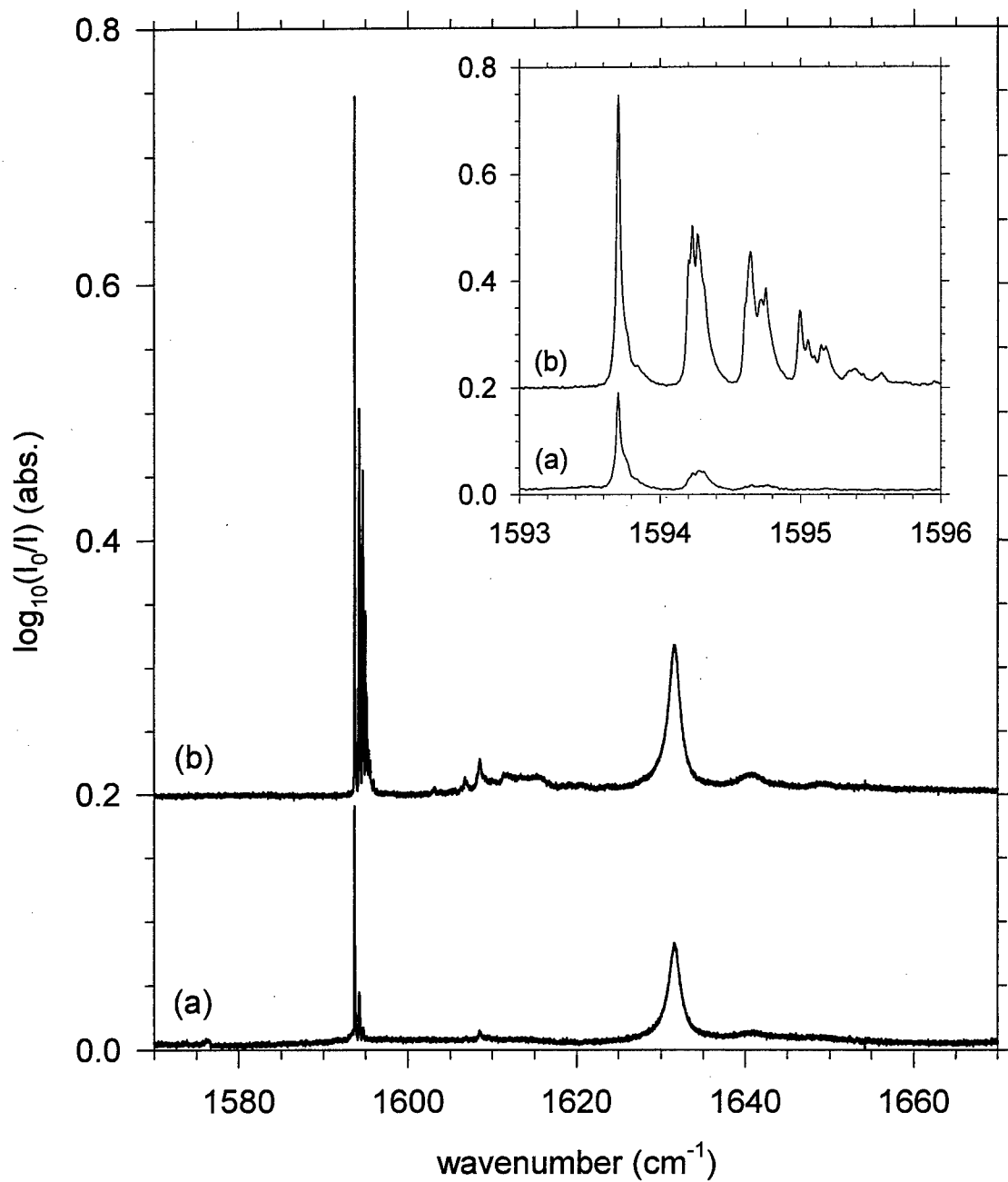


FIG. 11. Fajardo, Tam, and DeRose.

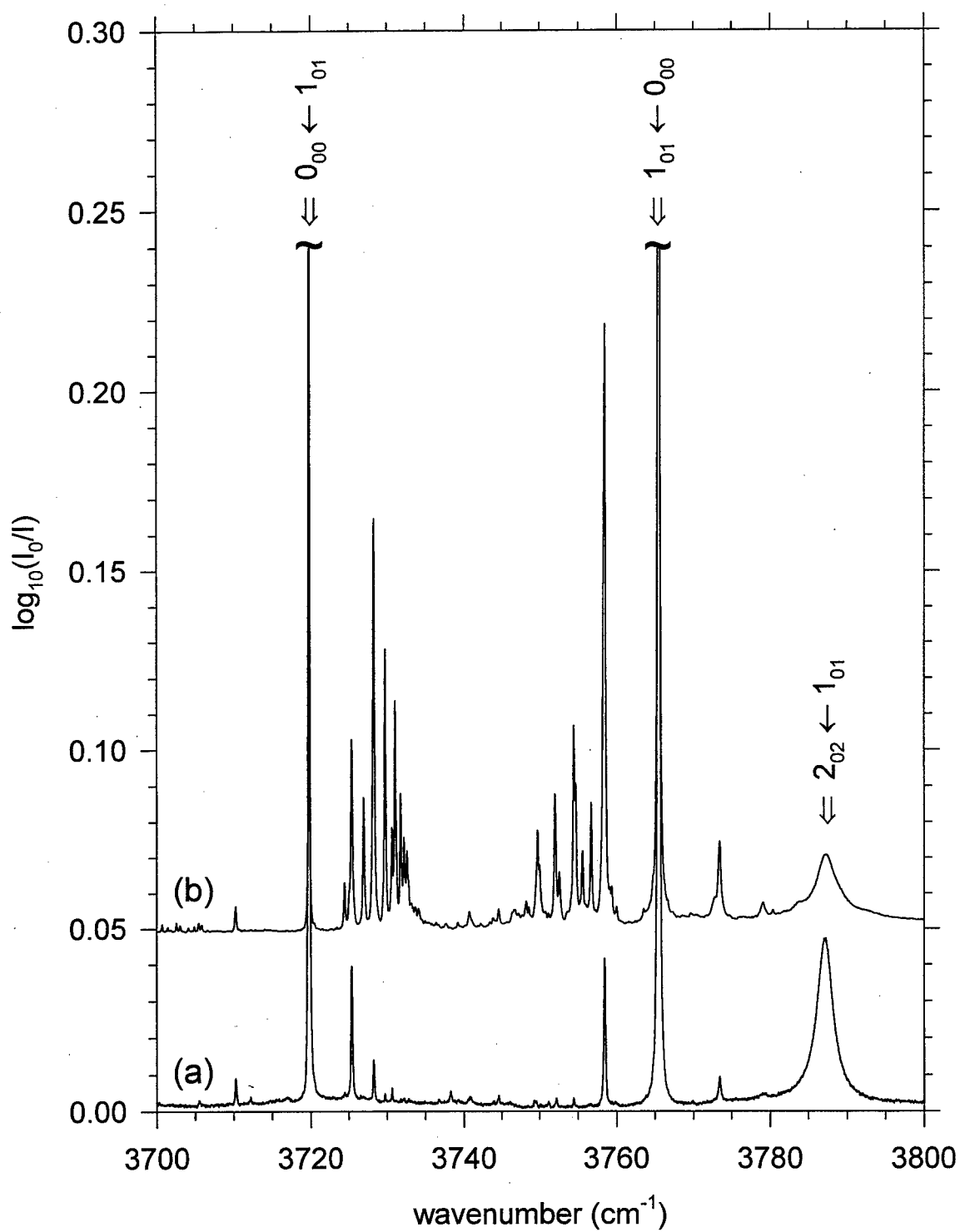


FIG. 12. Fajardo, Tam, and DeRose.

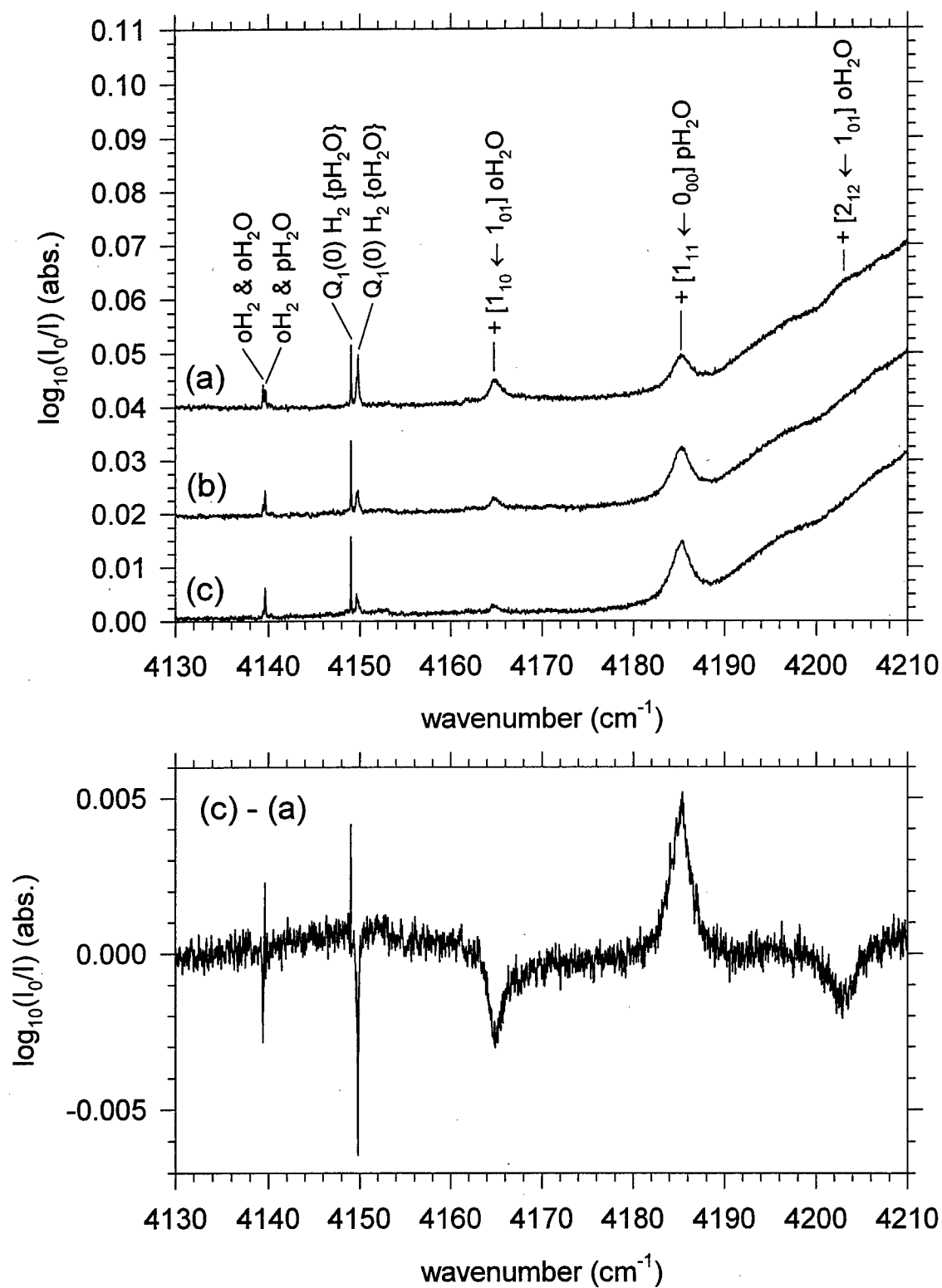


FIG. 13. Fajardo, Tam, and DeRose.

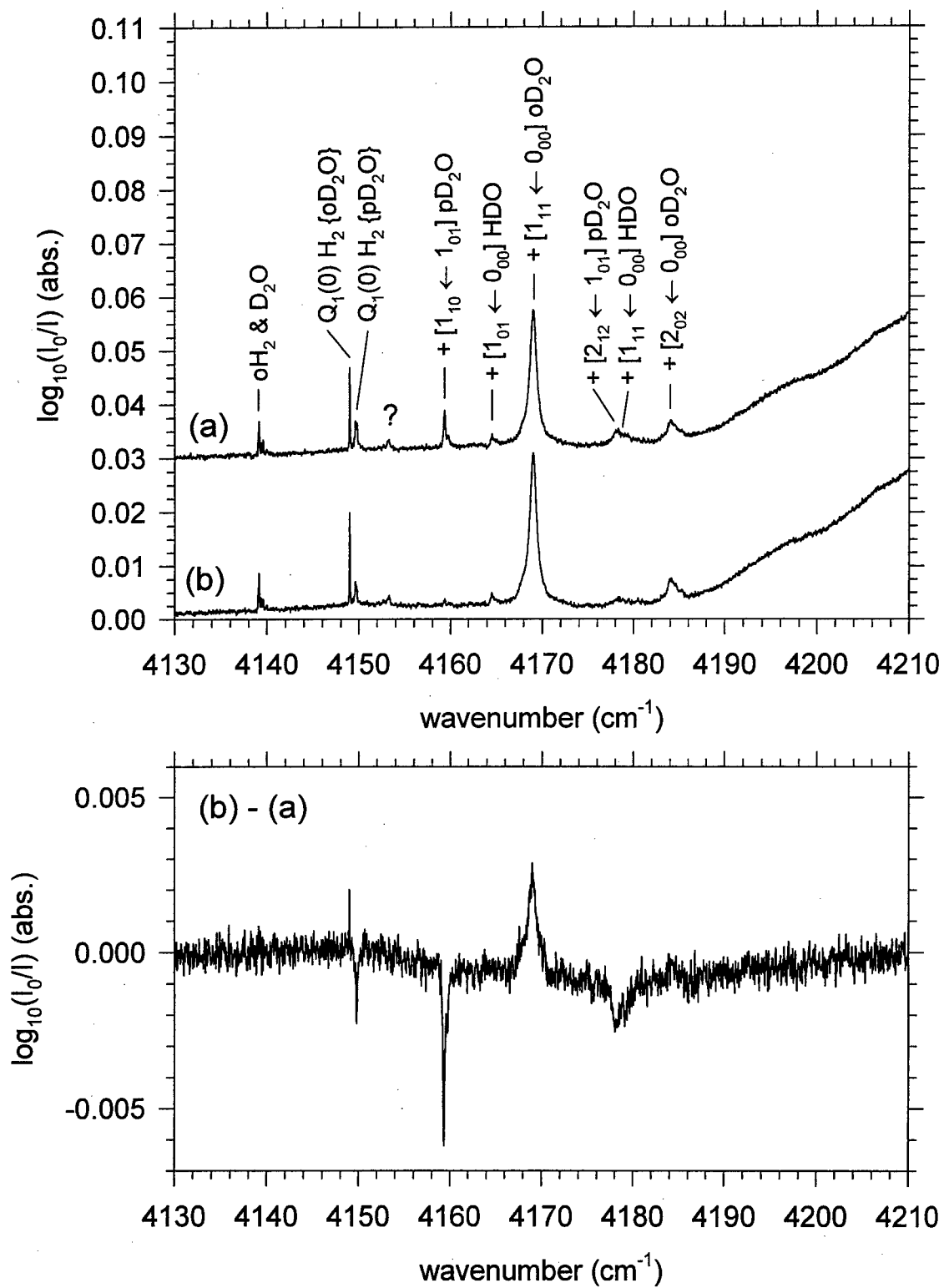


FIG. 14. Fajardo, Tam, and DeRose.